Kinematics of flagellar swimming in *Euglena gracilis*: Helical trajectories and flagellar shapes

Massimiliano Rossi[a,b,1], Giancarlo Cicconofri[a,1], Alfred Beran[c], Giovanni Noselli[a], and Antonio DeSimone[a,2]

[a]MathLab, International School for Advanced Studies, 34136 Trieste, Italy; [b]Institute of Fluid Mechanics and Aerodynamics, Bundeswehr University Munich, 85577 Neubiberg, Germany; and [c]Sezione Oceanografia, Istituto Nazionale di Oceanografia e di Geofisica Sperimentale, 34151 Trieste, Italy

Edited by David A. Weitz, Harvard University, Cambridge, MA, and approved October 16, 2017 (received for review May 16, 2017)

The flagellar swimming of euglenids, which are propelled by a single anterior flagellum, is characterized by a generalized helical motion. The 3D nature of this swimming motion, which lacks some of the symmetries enjoyed by more common model systems, and the complex flagellar beating shapes that power it make its quantitative description challenging. In this work, we provide a quantitative, 3D, highly resolved reconstruction of the swimming trajectories and flagellar shapes of specimens of *Euglena gracilis*. We achieved this task by using high-speed 2D image recordings taken with a conventional inverted microscope combined with a precise characterization of the helical motion of the cell body to lift the 2D data to 3D trajectories. The propulsion mechanism is discussed. Our results constitute a basis for future biophysical research on a relatively unexplored type of eukaryotic flagellar movement.

Euglena gracilis | microswimmers | microscopy imaging | 3D flagellum shapes | helical trajectories

Euglenids have long been used as model organisms for a broad range of biological studies, possibly because of their unique taxonomic position, which shows both animal-like and plant-like characteristics (1). Among the first microorganisms to be studied under a microscope (by van Leeuwenhoek, in the late 1600s), they still occupy center stage in contemporary research (2, 3), with new monographs soon to appear (4).

Studies on euglenid motility have recently focused on metaboly (5, 6), while flagellar swimming remains poorly investigated and understood, at least from the quantitative point of view. Qualitative observations have been made about the wiggling motion of the euglenid flagellum. Its characteristic movement has been dubbed "spinning lasso" or "figure eight." A quantitative description of this peculiar movement, whose primary source of activation is the "9 + 2" axoneme common to most eukaryotes (7), is still lacking. Reconstruction of the flagellar motion and actuation of euglenids faces a major challenge: capturing the complex 3D configurations of the flagellum, which evades the inquiry of current microscopy techniques. Planar beats of flagella, easier to capture from image data, are otherwise widely studied (8–11).

A typical specimen of *Euglena gracilis* (Fig. 1*A*) is around 50 μm in length. The flagellum they use for locomotion, which is slightly shorter than its body, beats by spinning at ∼40 Hz in close proximity to the cell body (Movie S1). As for most flagellates, the swimming motion of *E. gracilis* is rototraslatory and inherently 3D. Whereas 3D tracking of swimming microorganisms is a long-standing experimental research field (12), and still developing, none of the current techniques is capable of capturing the flagellar swimming of euglenids in full detail. For example, stereomatching has been used to track euglenids and other protists (13, 14), but it lacks the spatial resolution to resolve the motion of both body and flagellum (the whole swimmer is a point). Confocal microscopy, a powerful tool for 3D imaging, does not have sufficient time resolution (15) to resolve flagellar beating. Digital holographic microscopy is capable of high resolution in both time and space (16), and it gives the possibility of multiple simultaneous tracking for high-throughput statistics (17, 18). However, to date it has been successful only up to the 3D reconstruction of trajectories and pitch of particle-like objects with a prolate shape (19) and of the helical beating of an isolated flagellar structure (20). The close proximity of *Euglena*'s flagellum to the cell body makes the simultaneous reconstruction of cell body and flagellar shape a challenge, even for this technique.

We are able to recover the flagellar kinematics of *E. gracilis* through a reconstruction strategy based on simple assumptions and on the physics governing the motion of the system. Our analysis is based on standard microscopy image sequences, recorded at high frame rate. This guarantees the appropriate spatiotemporal resolution (even though from a 2D perspective). We restrict our analysis to the case in which the *Euglena* flagellar beating is, to a good approximation, periodic in time (hence, no lateral steering).

In this case, the physics governing the system (low Reynolds number hydrodynamics) imposes restrictions on which trajectories and rotations of the cell are actually possible.

Swimming at Low Reynolds Number with Periodic Beats

Helical swimming trajectories are ubiquitous among microorganisms (21). Simple physical arguments can explain the prevalence of helical trajectories, as suggested in the seminal papers (22, 23). The homogeneity and isotropy of fluid–body hydrodynamic interactions, which hold true for a body isolated from boundaries or other objects, play a crucial role. In this case, the

Significance

Active flagella provide the propulsion mechanism for a large variety of swimming eukaryotic microorganisms, from protists to sperm cells. Planar and helical beating patterns of these structures are recurrent and widely studied. The fast spinning motion of the locomotory flagellum of the alga *Euglena gracilis* constitutes a remarkable exception to these patterns. We report a quantitative description of the 3D flagellar beating in swimming *E. gracilis*. Given their complexity, these shapes cannot be directly imaged with current microscopy techniques. We show how to overcome these limitations by developing a method to reconstruct in full the 3D kinematics of the cell from conventional 2D microscopy images, based on the exact characterization of the helical motion of the cell body.

Author contributions: M.R., G.N., and A.D. designed research; M.R., G.C., G.N., and A.D. performed research; M.R. analyzed data; M.R. and G.N. designed experiments; A.B. grew cells and shared expertise on microscopy; G.C. and A.D. developed the theoretical model; and M.R., G.C., A.B., G.N., and A.D. wrote the paper.

The authors declare no conflict of interest.

This article is a PNAS Direct Submission.

[1]M.R. and G.C. contributed equally to this work.

[2]To whom correspondence should be addressed. Email: desimone@sissa.it.

This article contains supporting information online at www.pnas.org/lookup/suppl/doi:10.1073/pnas.1708064114/-/DCSupplemental.

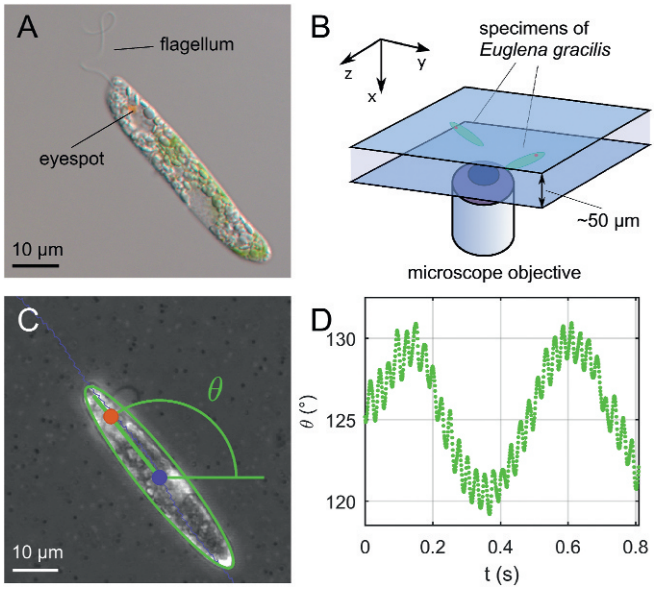

Fig. 1. (*A*) Micrograph of a specimen of *E. gracilis*. The anterior flagellum is visible, together with the eyespot, a pigmented organelle that is part of the photosensory apparatus of the cell. (*B*) Schematic of the experimental setup: Euglenids swim between two microscope slides separated by ∼50 μm. (*C*) Example of image segmentation results from high-speed videos: Position of the geometric body center (blue), position of the eyespot (red), and body orientation (green) are measured. (*D*) Projected body orientation θ as a function of time: A large amplitude oscillation is modulated by a smaller oscillation at flagellar beating time scale.

periodic beating of a swimmer results in periodic body frame components of its translational and angular velocities. See *Supporting Information*, section 1 for details. The time evolution of the center $\mathbf{c}$ and of the rotation $\mathbf{R}$ of the swimmer body frame are obtained, via time integration, from these periodic velocities (Eq. **S7**). The general solution of the swimming problem driven by periodic beats, with period T_b, is as follows. The position of the body center $\mathbf{c}(t)$ evolves in time according to

$$\mathbf{c}(t) = \mathbf{c}_h(t) + \mathbf{R}_\mathbf{n}(\omega t)\tilde{\mathbf{c}}_b(t) \qquad [1]$$

while the rotation of the body is described by

$$\mathbf{R}(t) = \mathbf{R}_\mathbf{n}(\omega t)\tilde{\mathbf{R}}_b(t)\,. \qquad [2]$$

In the previous two formulas, the closed curve $\tilde{\mathbf{c}}_b$ and the rotation $\tilde{\mathbf{R}}_b$ are periodic functions, with period T_b, $\mathbf{R}_\mathbf{n}(\omega t)$ is a rotation with axis $\mathbf{n}$ and angle ωt, and $\mathbf{c}_h$ describes a circular helix with axis $\mathbf{n}$ that closes a turn every $T = 2\pi/|\omega|$ seconds. The details of the derivation of Eqs. **1** and **2** are given in the *Supporting Information*, section 1.

Two time scales emerge in defining the kinematics: the flagellar beating period T_b and the time T needed to close one turn of the smooth circular helix $\mathbf{c}_h$. In the swimming of *Euglena*, as for most microorganism, T is much larger then T_b: It takes many beats to close a turn. The general trajectory can be seen as a smooth—and "slow"—helix perturbed by T_b-periodic "fast" swirls. Similarly, the orientation of the body can be seen as a slow rotation with constant angular velocity around $\mathbf{n}$, perturbed by fast T_b-periodic jerks.

Translational and rotational motions are coupled. For the sake of argument, suppose that $T = NT_b$ is a multiple of T_b. Then, fix a phase τ within one beat and consider times $t_k = \tau + kT_b$. The center moves according to $\mathbf{c}(t_k)$, and these points lie on a circular helix of axis $\mathbf{n}$ (a perturbed version of $\mathbf{c}_h$: a helix with the same pitch, but possibly different radius). Meanwhile, the body of the swimmer keeps rotating around the axis $\mathbf{n}$, each time by an angle $\omega T/N$. It follows that after N beats, exactly when one turn of the helix is closed, the swimmer ends up in the same orientation (Movie S2).

Results from recent studies on 3D helical trajectories of microswimmers can be cast within the predictions of this model. Observed "chiral ribbon" trajectories in human sperm motility (18) fall precisely in the general expression given by Eq. **1**. In the chiral ribbon case, the periodic $\tilde{\mathbf{c}}_b$ traces a line segment, a special and degenerate case of our more general $\tilde{\mathbf{c}}_b$, which describes a closed orbit. Rather than lying on a ribbon, the resulting *Euglena*'s trajectories are drawn on a "helically shaped tube" (a tubular neighborhood of the "backbone" helix $\mathbf{c}_h$). We emphasize that Eqs. **1** and **2** provide the general characterization for any motion driven by the periodic beating of a propulsive appendage. Special cases, where the backbone curve $\mathbf{c}_h$ of the trajectory in Eq. **1** is either a planar curve, or a straight line, follow when the rotation axis $\mathbf{n}$ is either orthogonal to the translation in one beat (as in the planar trajectories of sperm cells, when propelled by planar beating of their tails) or parallel to it (as in the case of bacteria propelled by rotating helical flagella).

Experimental Observations

We observed specimens of *E. gracilis* swimming in a water solution while confined between two microscope slides (Fig. 1*B*). The spacing between the slides was measured by focusing control beads attached to the respective walls (24) and was found to range between 40 and 60 μm. The control beads were also used to check that the fluid was at rest during the experiments. We acquired high-speed micrographs of several cells at 1,000 frames per second (fps), selecting only specimens swimming with a regular, periodic beat (Fig. 1*C*). More details about the experimental setup can be found in *Materials and Methods*.

In these conditions, for time scales larger than the flagellar beat, the swimming trajectories follow a characteristic sinusoidal path, while the cell body undergoes an apparent "swinging" movement with the same period. At smaller time scales, finer features of the trajectories can be observed, together with a higher-frequency "swinging" motion of the cell body (Movie S1). The latter becomes evident by plotting the projected body orientation as a function of time (Fig. 1*D*): A fast oscillation with amplitude $\sim 1^\circ$ and period ~ 25 ms is superimposed on a slower oscillation with amplitude $\sim 5^\circ$ and period ~ 0.5 s. This is the typical footprint of a helical swimming motion projected on a 2D plane.

Cell Body Motion Reconstruction

Eqs. **1** and **2** can be applied to recover 3D kinematics from 2D image sequences. This can be achieved by fitting 2D projections of the 3D kinematics imposed by theory to experimental data. A similar idea has been pursued in refs. 25–27. In the following, we outline the main steps of our procedure.

We model *Euglena*'s body as an ellipsoid (in our experiments, the surface of the cell does not visibly deform during swimming). We consider the swimmer reference frame located at the geometric center of the body, with axes aligned with the symmetry axes of the ellipsoid. With optical aberrations and out-of-focus effects being negligible, microscopy images of the cell body can be assimilated to projections of the ellipsoid on the focal plane. Using image segmentation, we extract three relevant kinematic quantities from these projections (Fig. 1*C*): the projection $\Pi\mathbf{c}$ of the body center (Fig. 2*E*), the projection $\Pi\mathbf{e}$ of the eyespot position $\mathbf{e}$ (Fig. 2*F*), and the angle θ, formed by the projection of the major axis of the ellipsoid with the horizontal (Fig. 2*G*).

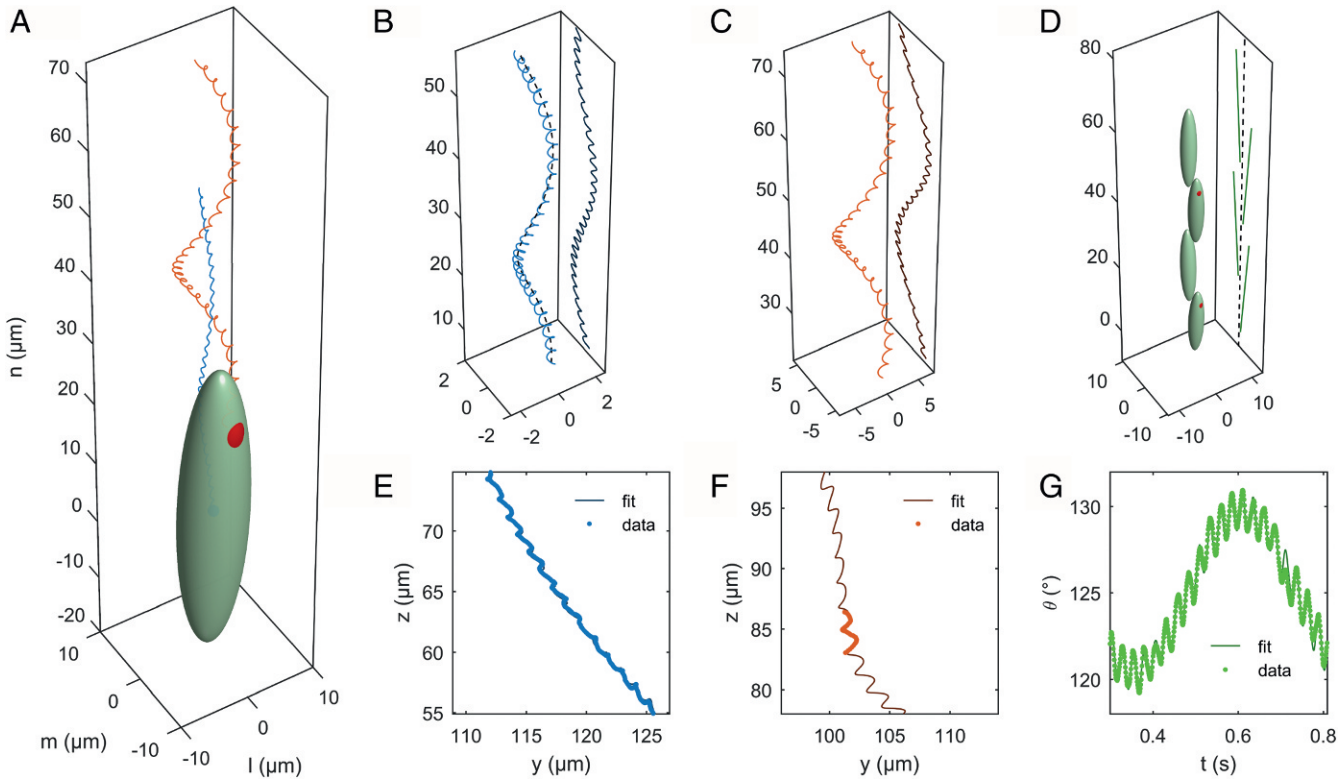

Fig. 2. (*A*) Three-dimensional representation of *Euglena*'s body, with trajectories of the body center (blue) and of the eyespot (red) reconstructed from the fitting procedure. The reference axes **l**, **m**, and **n** are chosen such that **n** is the axis of the helical trajectory. (*B*) Projection of the centroid trajectory $\Pi\mathbf{c}$ and (*C*) of the eyespot trajectory $\Pi\mathbf{e}$ on the focal plane. (*D*) Projection of the major axis of the cell body $\Pi\mathbf{k} = (\cos\theta, \sin\theta)$ on the focal plane. (*E*–*G*) Comparison between experimental measurements and model best-fitting curves for the quantities $\Pi\mathbf{c}$, $\Pi\mathbf{e}$, and θ. Note that the experimental data for $\Pi\mathbf{e}$ are available only when the eyespot is visible.

We then consider the restrictions imposed by the theoretical model and obtain formulas for the observable quantities $\Pi\mathbf{c}$, $\Pi\mathbf{e}$, and θ. They depend on a list of parameters ξ, which include, among others, the beating period T_b, the Fourier coefficients of the T_b-periodic functions in Eqs. **1** and **2**, and the geometric parameters of the circular helix $\mathbf{c}_h$. For the full list ξ of parameters, and their detailed expressions, we refer the reader to *Supporting Information*, section 2.

We recover the values of the parameters ξ by finding the least-squares fit between theoretical observables and measured experimental data. That is, we find ξ that minimizes

$$\sum_j \|\Pi\mathbf{c}(\xi, t_j^c) - \Pi\mathbf{c}^*(t_j^c)\|^2,$$

$$\sum_j \|\,\Pi\mathbf{e}(\xi, t_j^e) - \Pi\mathbf{e}^*(t_j^e)\,\|^2, \text{ and } \sum_j \left|\theta(\xi, t_j^\theta) - \theta^*(t_j^\theta)\right|^2,$$

where the ξ-dependent functions are the expression given by the theory for $\Pi\mathbf{c}$, $\Pi\mathbf{e}$, and θ, while experimental data are denoted with an asterisk. Sums are taken over the time instants where tracking data are available.

The set of parameters ξ so obtained is sufficient to determine the 3D expression for **c** and **R** as given by Eqs. **1** and **2**, thus allowing us to recover the full 3D time evolution of the reference frame of the swimmer (Fig. 2*A*).

The fact that $\Pi\mathbf{c}$, $\Pi\mathbf{e}$, and θ contain all of the information needed to recover the 3D kinematics becomes evident when going through the details of the theory, for which we refer to *Supporting Information*, section 2. We mention here the key ideas behind this. The time evolution of $\Pi\mathbf{c}$ alone is sufficient to recover the 3D trajectory of **c** (Fig. 2*B*). The "lift" $\Pi\mathbf{c} \to \mathbf{c}$ is possible thanks to the rotational symmetry imposed by Eq. **1**. Similarly, the angle θ is sufficient to lift $\Pi\mathbf{k} \to \mathbf{k}$ the projection $\Pi\mathbf{k} = (\cos\theta, \sin\theta)$ of the unit vector **k** that determines the major symmetry axis of the cell body in 3D (Fig. 2*D*). The extra datum $\Pi\mathbf{e}$ contains the information about the cell body rotation around **k**. Together with θ, the eyespot projection allows us then to recover the whole swimmer moving frame, that is, $(\theta, \Pi\mathbf{e}) \to \mathbf{R}$.

Flagellar Shapes

We reconstruct the shapes of the flagellum, that is, the time history of a 3D deformable curve, from the knowledge of its (partial) projections given by microscopy images. The reconstruction consists of finding a curve minimizing a "projection error," which quantifies the distance between experimental points and projections of the curve. We describe the method in more detail in the following.

Fix a phase τ between 0 and T_b (determined earlier) and consider images at times $t_k = \tau + kT_b$. At these instants, assuming beat periodicity, the flagellum lies in the same configuration with respect to the body frame. As the *Euglena* rotates, for different t_k a different view of this configuration appears on the focal plane. The results of the previous section allow us to locate at every instant the focal plane with respect to the body frame. Image segmentation gives us a set of points where the flagellum projection on each plane must lie (Fig. 3*A*).

We are able to locate N_{pl} planes (11 to 19, depending on the experiment) together with a set of projection points P_j^* for each plane $j = 1, 2, \ldots, N_{pl}$. The flagellum is recovered by finding the 3D curve whose projections are the closest possible to these sets of experimental points on the respective planes (Fig. 3*B*

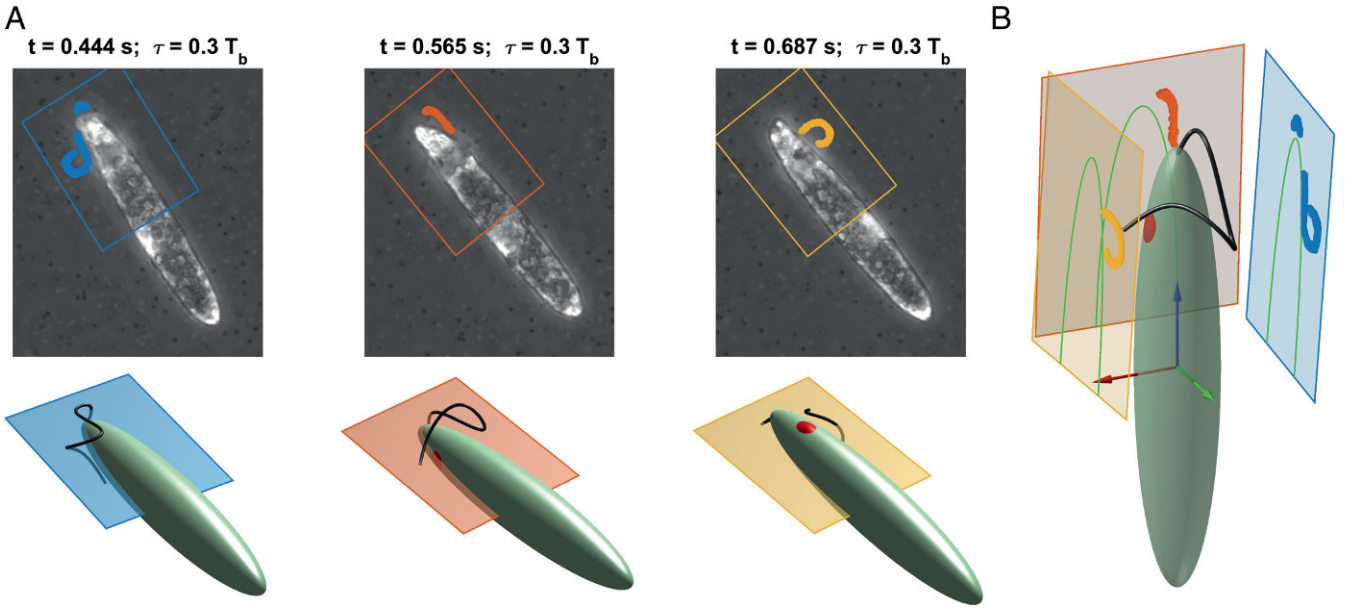

Fig. 3. Stereographic reconstruction of the flagellum. (*A*) Fixed a phase τ between 0 and the beating period T_b, images taken at times $t_k = \tau + kT_b$, show the flagellum in the same configuration with respect to the cell body, but from different viewpoints (*Top*). At each instant the *Euglena*'s position and orientation with respect to the focal plane are known from 3D cell body motion reconstruction results (*Bottom*). (*B*) The flagellum is recovered by finding the 3D curve whose projections (on the respective planes) are the closest possible to the experimental projections.

and Movie S3). The "closeness" of a curve $\mathbf{r}$ to the experimental points is determined by the projection error

$$Err(\mathbf{r}) = \sum_{j=1}^{N_{pl}} \sum_{\mathbf{p}^* \in P_j^*} \mathrm{dist}(\mathbf{p}^*, \Pi_j \mathbf{r})^2, \qquad [3]$$

where we denoted by Π_j the projection on the jth plane. In the previous equation, the distance dist $(\mathbf{p}^*, \Pi_j \mathbf{r})$ between a point $\mathbf{p}^*$ and the projection $\Pi_j \mathbf{r}$ is defined as the minimum with respect to the curve parameter s of $\| \mathbf{p}^* - \Pi_j \mathbf{r}(s) \|$. We use interpolating cubic spline curves

$$\mathbf{r} = Sp(\mathbf{x}_1, \ldots, \mathbf{x}_{N_{sp}}) \qquad [4]$$

to parametrize the flagellum. The interpolated points $\mathbf{x}_1, \ldots, \mathbf{x}_{N_{sp}}$ are chosen as to minimize the projection error. Substituting Eq. **4** in Eq. **3** leads to the expression to be minimized. More details on the algorithmic implementation of the problem are given in *Supporting Information*, section 3.

Results

Motion Characteristics. We applied our technique to multiple sets of experimental data, obtaining excellent agreement between experiments and theory (Fig. 2 *E* and *F*). We report here on the reconstruction of trajectories and flagellar shapes for one representative cell. Results for other cells are reported in *Supporting Information,* section 4, with comments on the variability of the results between different cells, and on the quantitative evaluation of the uncertainties of our reconstruction procedures. In particular (Fig. 4 and Movie S4), the history of flagellar shapes of our representative cell matches well with those of different specimens, suggesting the existence of a distinctive *Euglena* beat style, as described below.

A side view of the reconstructed swimming kinematics is shown in Fig. 5*A*. For visualization purposes, the *Euglena*'s body is not to scale with the displacements. The trajectory of the body center evolves along a helix with right-handed orientation. The helix is actually quite narrow, with an average radius of ≈0.75 μm, a small fraction of the *Euglena*'s width of ∼9.2 μm. The pitch is ≈35.8 μm, ∼0.7 times the length of the cell ∼50.8 μm. The calculated beating period is $T_b \approx 24.3$ ms. The *Euglena* closes a turn of the helix in $T \approx 0.5$ s, so approximately after $N = 21$ beats. In Fig. 5*B* a top view of the trajectory is shown. A color map on the trajectory displays the absolute velocity of the body center: The center moves by continuously accelerating and decelerating, with velocities ranging between 50 and 140 μm/s. The cell body (full or transparent) is depicted at the beginning of each beat ($\tau = 0$). It can be noticed that the eyespot points in the outward direction.

To have a closer picture of the periodic motion within one beat we consider the evolution of the system as seen by an observer

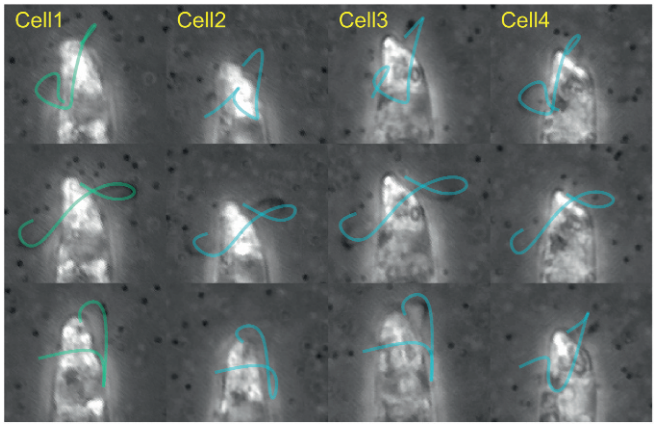

Fig. 4. Grid of experimental images from four different swimming cells (columns) taken at different times (rows). The reconstructed time history of flagellar shapes from cell 1 (green, first column), conveniently scaled in both space and time, is attached to the other cells' bodies (blue). A good overlap between the projections of the attached flagella and the experimental images emerges (see Movie S4 and *Supporting Information*, section 4 for more details). This shows that the flagellar beat of cell 1, presented here in the main text, is a valid representative of a common beating style.

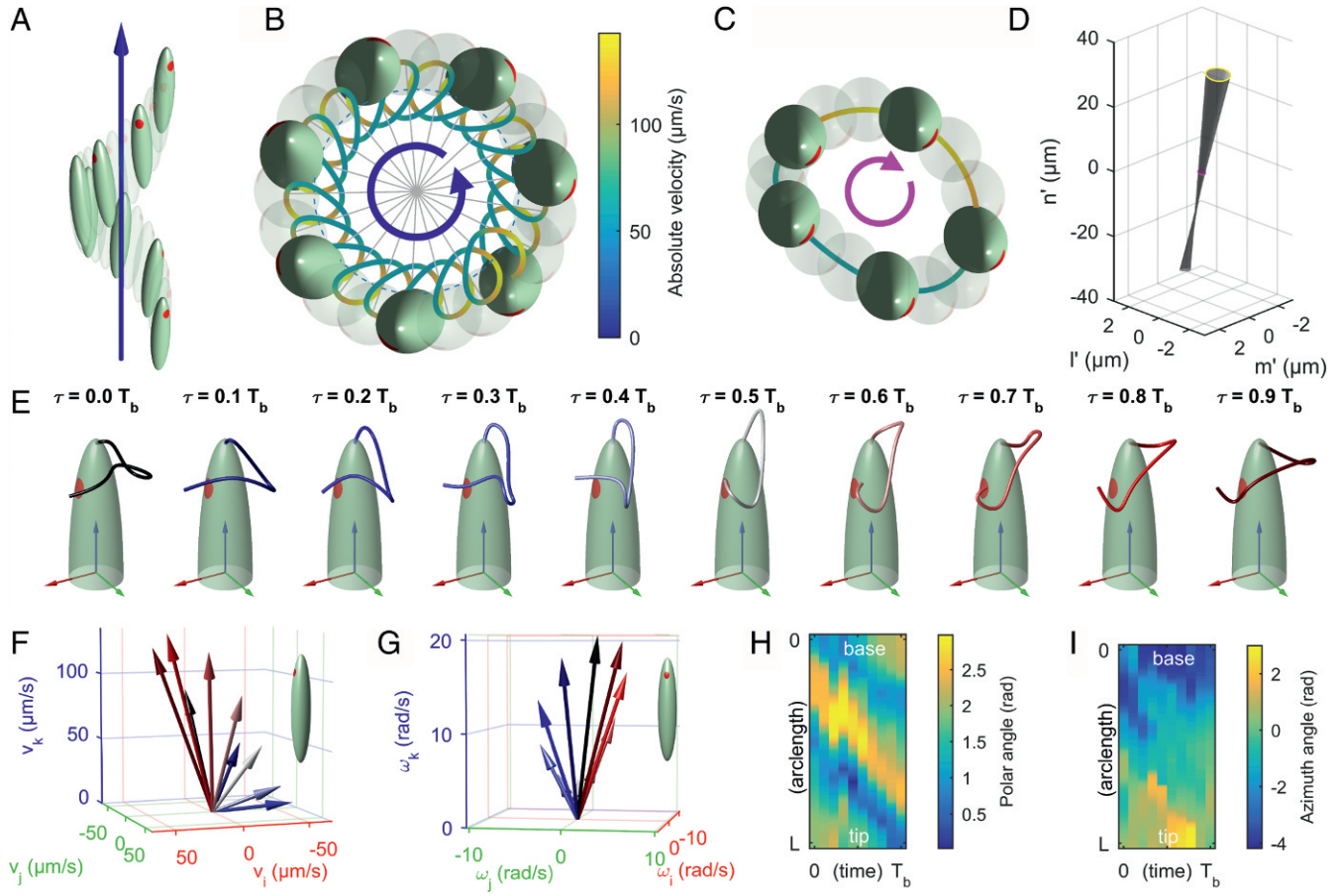

Fig. 5. (*A–D*) Representation of *Euglena*'s kinematics. The dimensions of the cell body are not to scale with displacements for visualization purposes. (*A*) Side view. The *Euglena* follows a right-handed helical path. Full or transparent bodies are shown at the beginning of each beat. (*B*) Top view. The body center trajectory $\mathbf{c}(t)$ is rendered using a color map to highlight the absolute instantaneous velocity. (*C*) Body motion as seen from a reference frame of axes $\mathbf{l}'$, $\mathbf{m}'$, and $\mathbf{n}'$ moving on the circular helix $\mathbf{c}_h(t)$ while rotating by $\mathbf{R}_\mathbf{n}(\omega t)$ (top view). Full or transparent bodies are shown at instants equally spaced within one beat. (*D*) Quasi-conical surface spanned by the major symmetry axis of the cell during one beat. (*E*) Sequence of flagellar shapes for 10 consecutive instants (phases) within one beat. Each phase is labeled with a different color. Body reference axes **i**, **j**, and **k** are represented in red, green, and blue, respectively. (*F*) Translational velocity **v** and (*G*) angular velocity $\boldsymbol{\omega}$ of the cell, represented in body reference frame coordinates. Velocities are shown for each flagellar phase and color-coded accordingly. (*H*) Polar angle and (*I*) azimuth angle of the unit tangent vector to the flagellum, as functions of the arc length and time.

moving with the backbone helix $\mathbf{c}_h(t)$ while rotating by $\mathbf{R}_\mathbf{n}(\omega t)$ (Eq. **1**). In this view (Fig. 5*C*), the cell moves on a quasi-circular orbit in clockwise direction (opposite to the one of the backbone trajectory). As for the body orientation, it is interesting to note that the surface spanned by the major symmetry axis of the cell is roughly a cone (Fig. 5*D*): The projection of this motion in 2D translates into the "small amplitude swings" observed at the microscope. The rotation around its long axis (so to say its "rolling" motion) is negligible and the eyespot points always to the same direction.

Remarks on the Propulsion Mechanism. A sequence of flagellar shapes for 10 consecutive instants (phases) within one beat is shown in Fig. 5*E*. In Fig. 5 *F* and *G* the resulting instantaneous translational and angular velocities are represented in body reference frame coordinates. Each phase is labeled with a different color. Bending waves emerge from the base of the flagellum and run through its whole length, fading at its tip. The flagellum bends while swinging around the cell body, with velocities that oscillate significantly both in magnitude and direction.

The propulsion mechanism of *Euglena* cannot be adequately summarized as a "backward beating of a flagellum to push the cell forward." The flagellum beats laterally, spanning a complex sequence of nonplanar shapes: No obvious symmetries can be exploited to guess the way the body moves as a result of the flagellar beating. In fact, this motion entails spiraling trajectories coupled to body rotations. To confirm that the reconstructed flagellar shapes are consistent with the observed swimming motion, we calculated the kinematics that the reconstructed flagellar beat generates by imposing the hydrodynamic force balance on the swimmer. Using the local drag approximation (28) of resistive force theory (RFT), we obtained a good qualitative agreement by fitting the resistive coefficients for the flagellum to best match the experimental data, as done in ref. 9 (*Supporting Information*, section 5 and Fig. S6). Reproducing the experimental data in full quantitative detail will require a more detailed analysis.

RFT shows that the observed kinematics is consistent with the typical thrust mechanism of smooth flagella. Indeed, peaks in the translational velocity of the cell body are correlated with the flagellar wave propagating parallel to the major axis, in the direction opposite to the one of motion, while peaks in the rotational velocity occur during the flagellar swing around the body (see Movie S5 and *Supporting Information*, section 5 for more details). This seems to confirm the claim (29) that, for the euglenoid flagellum, the presence of soft (nontubular) mastigonemes does not

affect the flagellar thrust mechanism in a major way, as it instead happens in other organisms (30).

Conclusions

We have presented a 3D kinematics reconstruction of euglenid flagellar motion. To accomplish this, we have introduced a technique to recover 3D kinematics from 2D microscopy images (Movie S6). This gives unprecedented detail, and it is applicable to other organisms.

As with other methods to reconstruct 3D information from 2D data (25–27), our approach is based on a model and on specific assumptions. In particular, we are limited to periodic beating and to motions confined to the narrow field of view of high-resolution microscopy. Even when these limitations will be overcome by new techniques capable of direct 3D imaging of flagellar and body kinematics (at comparable levels of spatiotemporal detail), the characterization of trajectories as generalized helices, on which our method is based, will stand. The biological significance of patterns emerging from the trajectories of flagellated unicellular swimmers has often been emphasized in the past (18). Here we show that, in fact, the geometric structure of the trajectories is exactly the signature of the periodic flagellar beating that generates them.

Our work paves the way for future studies of the flows induced in the surrounding fluid by flagellar beating and for the investigation of the mechanisms governing the internal actuation of the flagellum. *E. gracilis* can be seen as a first example for a large class of model organisms whose swimming strokes are less symmetric than those explored so far and for which quantitative data are not yet available.

Materials and Methods

Cell Culture. Strain SAG 1224-5-27 of *E. gracilis* obtained from the SAG Culture Collection of Algae at the University of Göttingen was maintained axenic in liquid culture medium Eg (see the medium recipe from SAG) in sterile 16-mL polystyrene test tubes. Cultures were transferred weekly. They were kept in an incubator (IPP 110plus; Memmert) at 15 °C and at a light: dark cycle of 12:12 h under cold white LED illumination with an irradiance of about 50 μmol/(m^{2}s).

Experimental Setting. For each experimental trial a dilute solution was prepared of *E. gracilis* and of 0.5 μm in diameter polystyrene, fluorescent beads [(F8813; Life Technologies), volume fraction of $\sim$0.05%] in culture medium Eg. Swimming cells were imaged in phase contrast illumination by using an Olympus IX81 inverted microscope equipped with a LCAch 40$\times$ Ph2 objective (N.A. 0.55). The estimated depth of field for such arrangement is $\sim$2.3 μm. Cells were confined between two microscope slides separated with a $\sim$50-μm-thick double-sided adhesive spacer. Micrographs were recorded at a frame rate of 1,000 fps by using a high-speed complementary metal–oxide–semiconductor digital camera (FASTCAM Mini UX100; Photron).

Image Processing and Data Fitting. Image processing and numerical fitting have been performed with programs developed in-house implemented in the MATLAB environment (MathWorks).

ACKNOWLEDGMENTS. This research was conducted at the International School for Advanced Studies (SISSA) SAMBA laboratory during several visits by M.R. This work was supported by SISSA and the European Research Council through AdG-340685 MicroMotility.

1. Buetow De (1982) *The Biology of Euglena: Physiology* (Academic, New York), Vol 3.
2. Lukes J, Leander BS, Keeling PJ (2009) Cascades of convergent evolution: The corresponding evolutionary histories of euglenozoans and dinoflagellates. *Proc Natl Acad Sci USA* 106(Suppl 1):9963–9970.
3. Triemer R, Zakrys B (2015) *Photosynthetic Euglenoids*, eds Wehr J, Sheath R, Kociolek J (Academic, New York), pp 457–482.
4. Schwartzbach S, Shigeoka S (2017) *Euglena: Biochemistry, Cell and Molecular Biology* (Springer, Berlin).
5. Arroyo M, Heltai L, Millán D, DeSimone A (2012) Reverse engineering the euglenoid movement. *Proc Natl Acad Sci USA* 109:17874–17879.
6. Arroyo M, DeSimone A (2014) Shape control of active surfaces inspired by the movement of euglenids. *J Mech Phys Sol* 62:99–112.
7. Manton I, Clarke G (1981) Cilia and flagella of eukaryotes. *J Cell Biol* 91:107s–124s.
8. Brokaw C, Luck D, Huang B (1982) Analysis of the movement of Chlamydomonas flagella: The function of the radial-spoke system is revealed by comparison of wild-type and mutant flagella. *J Cell Biol* 92:722–732.
9. Friedrich B, Riedel-Kruse I, Howard J, Jülicher F (2010) High-precision tracking of sperm swimming fine structure provides strong test of resistive force theory. *J Exp Biol* 213:1226–1234.
10. Geyer V, Jülicher F, Howard J, Friedrich B (2013) Cell-body rocking is a dominant mechanism for flagellar synchronization in a swimming alga. *Proc Natl Acad Sci USA* 110:18058–18063.
11. Leptos K, et al. (2013) Antiphase synchronization in a flagellar-dominance mutant of Chlamydomonas. *Phys Rev Lett* 111:158101.
12. Berg HC (1971) How to track bacteria. *Rev Sci Instrum* 42:868–871.
13. Thar R, Blackburn N, Kühl M (2000) A new system for three-dimensional tracking of motile microorganisms. *Appl Environ Microbiol* 66:2238–2242.
14. Drescher K, Leptos KC, Goldstein RE (2009) How to track protists in three dimensions. Review of scientific instruments 80:014301.
15. Jonkman J, Brown CM (2015) Any way you slice it-a comparison of confocal microscopy techniques. *J Biomol Tech JBT* 26:54–65.
16. Jikeli JF, et al. (2015) Sperm navigation along helical paths in 3D chemoattractant landscapes. *Nature Commun* 6:7985.
17. Su TW, Xue L, Ozcan A (2012) High-throughput lensfree 3D tracking of human sperms reveals rare statistics of helical trajectories. *Proc Natl Acad Sci USA* 109:16018–16022.
18. Su TW, et al. (2013) Sperm trajectories form chiral ribbons. *Nat Sci Rep* 3: 1664.
19. Bianchi S, Saglimbeni F, Di Leonardo R (2017) Holographic imaging reveals the mechanism of wall entrapment in swimming bacteria. *Phys Rev X* 7:011010.
20. Wilson LG, Carter LM, Reece SE (2013) High-speed holographic microscopy of malaria parasites reveals ambidextrous flagellar waveforms. *Proc Natl Acad Sci USA* 110:18769–18774.
21. Crenshaw HC (1996) A new look at locomotion in microorganisms: Rotating and translating. *Am Zoologist* 36:608–618.
22. Purcell EM (1977) Life at low Reynolds number. *Am J Phys* 45:3–11.
23. Shapere A, Wilczek F (1989) Geometry of self-propulsion at low reynolds number. *J Fluid Mech* 198:557–585.
24. Rossi M, Segura R, Cierpka C, Kähler C (2012) On the effect of particle image intensity and image preprocessing on the depth of correlation in micro-piv. *Exp Fluids* 52:1063–1075.
25. Gurarie E, Grünbaum D, Nishizaki MT (2011) Estimating 3D movements from 2D observations using a continuous model of helical swimming. *Bull Math Biol* 73: 1358–1377.
26. Bukatin A, Kukhtevich I, Stoop N, Jörn Dunkel J, Kantsler V (2015) Bimodal rheotactic behavior reflects flagellar beat asymmetry in human sperm cells. *Proc Natl Acad Sci USA* 112:15904–15909.
27. Carroll TJ (2015) *3D reconstruction of human sperm kinematics. Senior thesis* (Tufts Univ, Medford, MA).
28. Lauga E, Powers TR (2009) The hydrodynamics of swimming microorganisms. *Rep Prog Phys* 72:096601.
29. Bouck G, Rogalski A, Valaitis A (1978) Surface organization and composition of euglena.II. flagellar mastigonemes. *J Cell Biol* 77:805–826.
30. Brennen C (1975) Locomotion of flagellates with mastigonemes. *J Mechanochemistry Cell Motil* 3:207–217.
31. Kim S, Karrila S (2013) *Microhydrodynamics: Principles and Selected Applications* (Courier Corp., North Chelmsford, MA).
32. Barnkob R, Kähler C, Rossi M (2015) General defocusing particle tracking. *Lab A Chip* 15:3556–3560.
33. Katz D, Blake J, Paveri-Fontana S (1975) On the movement of slender bodies near plane boundaries at low Reynolds number. *J Fluid Mech* 72:529–540.

Supporting Information

Rossi et al. 10.1073/pnas.1708064114

1. Low Reynolds Number Swimming with Periodic Beats: Derivation of the Evolution Equations

We show here how to derive Eqs. **1** and **2** of the main text, starting from basic laws of low Reynolds number physics. The motion of a swimmer is determined by a map Φ_t defined on a set $\mathcal{B}$, the reference body, with values in $\mathcal{B}_t$, the body of the swimmer at time t. We can write

$$\Phi_t = \mathbf{c}(t) + \mathbf{R}(t)\bar{\Phi}_t, \qquad \textbf{[S1]}$$

where $\mathbf{c}(t)$ is the center of a reference frame moving with the body and $\mathbf{R}(t)$ determines the rotation of the moving frame. The map $\bar{\Phi}_t$ defines the shape of the swimmer at every t, assumed to be periodic with period T_b.

Given a periodic $\bar{\Phi}_t$, the time evolution of $\mathbf{c}(t)$ and $\mathbf{R}(t)$ are determined by the swimmer–fluid hydrodynamic interaction. The total force $\mathbf{f}$ and the total moment $\mathbf{g}$ (with respect to $\mathbf{c}$) exerted by the fluid on the swimmer are

$$\mathbf{f} = \int_{\partial\mathcal{B}_t} \mathbf{S}\boldsymbol{\nu}\, dA \quad \text{and} \quad \mathbf{g} = \int_{\partial\mathcal{B}_t} (\mathbf{x}-\mathbf{c}) \times \mathbf{S}\boldsymbol{\nu}\, dA, \qquad \textbf{[S2]}$$

where $\mathbf{S}$ is the stress tensor in the fluid and $\boldsymbol{\nu}$ denotes the outer unit normal to the boundary $\partial\mathcal{B}_t$ of the swimmer's body $\mathcal{B}_t$. By neglecting the swimmer's inertia, the equations of motion for the swimmer are given by

$$\mathbf{f} = \mathbf{0} \quad \text{and} \quad \mathbf{g} = \mathbf{0}. \qquad \textbf{[S3]}$$

The stress tensor $\mathbf{S}$ is determined by the (Eulerian) velocity field of the fluid $\mathbf{u}(\mathbf{x}, t)$ at $\partial\mathcal{B}_t$, and the associated pressure. We write $\mathbf{S}[\mathbf{u}]$ to denote the stress tensor associated with the field $\mathbf{u}$. From the no-slip boundary condition $\mathbf{u} = d\Phi_t/dt \circ \Phi_t^{-1}$ and Eq. **S1** we have

$$\mathbf{u}(\mathbf{x}, t) = \mathbf{v} + \boldsymbol{\omega} \times (\mathbf{x}-\mathbf{c}) + \mathbf{R}\,\frac{d\bar{\Phi}_t}{dt} \circ \bar{\Phi}_t^{-1}\left(\mathbf{R}^T(\mathbf{x}-\mathbf{c})\right) \qquad \textbf{[S4]}$$

for every point $\mathbf{x}$ in $\partial\mathcal{B}_t$, where $\mathbf{v}$ and $\boldsymbol{\omega}$ are the translational and angular velocity of the moving reference frame, respectively. For low Reynolds number flows, the stress tensor is linear with respect to the boundary velocity argument $\mathbf{u}$. We suppose that the resulting stress tensor has the following property (homogeneity and isotropy):

$$\mathbf{S}[\mathbf{u}] \circ \mathcal{R} = \mathbf{R}\mathbf{S}\left[\mathbf{R}^T\mathbf{u} \circ \mathcal{R}\right]\mathbf{R}^T, \qquad \textbf{[S5]}$$

where we have denoted by $\mathcal{R}$ the rigid transformation $\mathcal{R}\mathbf{x} = \mathbf{c} + \mathbf{R}\mathbf{x}$. Property **S5** is satisfied, for example, in the case of a single swimmer moving in a homogeneous and isotropic fluid occupying the whole 3D ambient space, and at rest at infinity. By making the hypothesis that Eq. **S5** holds also in our concrete experimental setup, we are assuming that the effects of walls and physical boundaries, of the presence of other swimmers, and so on, are, in fact, negligible.

Plugging the expression in Eq. **S4** into $\mathbf{S}[\mathbf{u}]$ and then in Eq. **S2**, using the property in Eq. **S5** together with the linearity of the stress tensor, we can rewrite (after some calculations) Eq. **S3** in the following way:

$$\begin{pmatrix}\bar{\mathbf{v}}\\ \bar{\boldsymbol{\omega}}\end{pmatrix} = -\begin{pmatrix}\bar{\mathbf{A}} & \bar{\mathbf{B}}\\ \bar{\mathbf{B}}^T & \bar{\mathbf{C}}\end{pmatrix}^{-1}\begin{pmatrix}\bar{\mathbf{f}}\\ \bar{\mathbf{g}}\end{pmatrix}, \qquad \textbf{[S6]}$$

where we have defined the translational $\bar{\mathbf{v}} = \mathbf{R}^T\mathbf{v}$ and angular $\bar{\boldsymbol{\omega}} = \mathbf{R}^T\boldsymbol{\omega}$ velocities as seen from the reference frame moving with the body. The t-dependent matrix in Eq. **S6** is (the inverse of) the "grand resistance matrix" (31) of the swimmer: It quantifies the viscous resistance to rigid motion of the swimmer at its current shape $\bar{\Phi}_t$. The vectors $\bar{\mathbf{f}}$ and $\bar{\mathbf{g}}$ are the force and moment that would act on the swimmer if it was held fixed at one point (and orientation), as a consequence of its shape change. All of the quantities in the right-hand side of Eq. **S6** depend only on $\bar{\Phi}_t$ and its time derivative. Hence, they are all T_b-periodic, which implies the periodicity of $\bar{\mathbf{v}}$ and $\bar{\boldsymbol{\omega}}$. From the definitions of $\bar{\mathbf{v}}$ and $\bar{\boldsymbol{\omega}}$ we have that

$$\frac{d\mathbf{c}}{dt}(t) = \mathbf{R}(t)\bar{\mathbf{v}}(t) \quad \text{and} \quad \frac{d\mathbf{R}}{dt}(t) = \mathbf{R}(t)[\bar{\boldsymbol{\omega}}(t)]_\times, \qquad \textbf{[S7]}$$

where $[\bar{\boldsymbol{\omega}}]_\times$ is the axial tensor of $\bar{\boldsymbol{\omega}}$ (defined as the skew-symmetric tensor such that $[\bar{\boldsymbol{\omega}}]_\times\mathbf{a} = \bar{\boldsymbol{\omega}} \times \mathbf{a}$ for every vector $\mathbf{a}$). Then, the evolution of the reference frame of a periodically beating swimmer must be the general solution of Eq. **S7**, where $\bar{\mathbf{v}}$ and $\bar{\boldsymbol{\omega}}$ are taken to be generic T_b-periodic vectors. In the remainder of this section we show that the integration of Eq. **S7** leads to Eqs. **1** and **2**.

From the second equation in Eq. **S7**, since $[\bar{\boldsymbol{\omega}}]_\times$ is T_b-periodic and skew-symmetric, we have that

$$\frac{d}{dt}\left(\mathbf{R}(t+T_b)\mathbf{R}(t)^T\right) = \mathbf{0}.$$

Thus, $\mathbf{R}(t+T_b)\mathbf{R}(t)^T$ is a t-independent rotation. We denote by $\mathbf{n}$ the unit vector determining the rotation axis of $\mathbf{R}(t+T_b)\mathbf{R}(t)^T$, and by $\Delta\psi$ the rotation angle. Using the same notations we have adopted in the main text we write

$$\mathbf{R}_\mathbf{n}(\Delta\psi) = \mathbf{R}(t+T_b)\mathbf{R}(t)^T, \quad \text{for every } t \geq 0. \qquad \textbf{[S8]}$$

Clearly, if $\mathbf{R}(t+T_b)\mathbf{R}(t)^T$ is the identity matrix we do not have a unique choice for $\mathbf{n}$. This is not the case for the rotatory motion of the *Euglena* studied here, so in the following we will assume that $\mathbf{n}$ is defined unambiguously and $\Delta\psi \neq 0$.

From Eq. **S8** it follows that $\mathbf{R}(t+kT_b) = \mathbf{R}_\mathbf{n}(k\Delta\psi)\mathbf{R}(t)$ for every integer $k \geq 0$. Therefore, if we consider

$$\tilde{\mathbf{R}}_b(t) := \mathbf{R}_\mathbf{n}(\Delta\psi\, t/T_b)^T\mathbf{R}(t), \qquad \textbf{[S9]}$$

we have (after a simple check) that $t \mapsto \tilde{\mathbf{R}}_b(t)$ describes a T_b-periodic rotation. Eq. **2** follows then from Eq. **S9** by taking $\omega = \Delta\psi/T_b$.

From the first equation in Eq. **S7** and the periodicity of $\bar{\mathbf{v}}$, and from Eq. **S8**, we have that

$$\frac{d}{dt}\Big(\mathbf{c}(t+T_b) - \mathbf{R}_\mathbf{n}(\Delta\psi)\mathbf{c}(t)\Big) = \mathbf{0}.$$

Then, there exists a t-independent vector $\mathbf{d}$ such that

$$\mathbf{d} = \mathbf{c}(t+T_b) - \mathbf{R}_\mathbf{n}(\Delta\psi)\mathbf{c}(t). \qquad \textbf{[S10]}$$

From Eq. **S10**, in particular, it follows that

$$\mathbf{c}(t+kT_b) = \begin{cases} \mathbf{c}(t) & \text{for } k=0, \\ \mathbf{d} + \mathbf{R}_\mathbf{n}(\Delta\psi)\mathbf{c}(t) & \text{for } k=1, \\ \sum_{j=0}^{k-1} \mathbf{R}_\mathbf{n}(j\Delta\psi)\mathbf{d} + \mathbf{R}_\mathbf{n}(k\Delta\psi)\mathbf{c}(t) & \text{for every integer } k>1. \end{cases} \qquad \textbf{[S11]}$$

If we define $\mathbf{d}_{//} := (\mathbf{d}\cdot\mathbf{n})\mathbf{n}$ and $\mathbf{d}_\perp := \mathbf{d} - \mathbf{d}_{//}$, after some algebra we can rewrite Eq. **S11** in closed form as

$$\mathbf{c}(t+kT_b) = \underbrace{\mathbf{R}_\mathbf{n}(k\Delta\psi)\mathbf{r}_\perp + \mathbf{d}_{//}k - \mathbf{r}_\perp}_{H_k} + \mathbf{R}_\mathbf{n}(k\Delta\psi)\mathbf{c}(t) \qquad \textbf{[S12]}$$

for every integer $k \geq 0$, with $\mathbf{r}_\perp := -(\mathbf{d}_\perp + \cot(\Delta\psi/2)\mathbf{n}\times\mathbf{d}_\perp)/2$ (notice that $\mathbf{r}_\perp$ is orthogonal to $\mathbf{n}$). Consider the expression H_k underlined by the curly brace in the right-hand side of Eq. **S12**. For every integer k, it gives a point that lies on a helix of axis parallel to $\mathbf{n}$ passing through the origin $\mathbf{o}$. We can parametrize such a helix with the t-dependent curve

$$\mathbf{c}_h^0(t) := \mathbf{R}_\mathbf{n}\left(\Delta\psi\, t/T_b\right)\mathbf{r}_\perp + \mathbf{d}_{//}\, t/T_b - \mathbf{r}_\perp.$$

A simple check shows that the curve $\tilde{\mathbf{c}}_b^0$ defined as

$$\tilde{\mathbf{c}}_b^0(t) := \mathbf{R}_\mathbf{n}(\Delta\psi\, t/T_b)^T\Big(\mathbf{c}(t) - \mathbf{c}_h^0(t)\Big)$$

is T_b-periodic. Thus, the general solution for $\mathbf{c}(t)$ of Eq. **S7** can be written as the sum of a helix $\mathbf{c}_h^0(t)$ and a term $\mathbf{R}_\mathbf{n}\left(\Delta\psi\, t/T_b\right)\tilde{\mathbf{c}}_b^0(t)$ where $\tilde{\mathbf{c}}_b^0$ is a T_b-periodic "swirl," as we called it in the main text. Eq. **1** then follows. We remark that there is not a unique choice for the helix and the swirl. Indeed, fix any constant vector $\mathbf{r}$ and take $\mathbf{c}_h(t) := \mathbf{c}_h^0(t) + \mathbf{R}_\mathbf{n}\left(\Delta\psi\, t/T_b\right)\mathbf{r}$ and $\tilde{\mathbf{c}}_b(t) := \tilde{\mathbf{c}}_b^0(t) - \mathbf{r}$. Clearly $\mathbf{c}_h$ is still a circular helix (same pitch, different radius) while $\tilde{\mathbf{c}}_b(t)$ is a T_b-periodic curve, and we have again Eq. **1**. However, when one helix is fixed, then the swirl is uniquely determined, and vice versa.

2. Cell Body Motion Reconstruction: Parametrization of the Moving Reference Frame and Data Fitting

In this section we give the detailed parametrization of the *Euglena*'s moving reference frame. We also provide more details on the data-fitting procedure (discussed in broad terms in the main text) used to reconstruct the 3D cell body kinematics from 2D microscopy images.

First, some definitions. We fix the laboratory frame as in Fig. S1: The $\mathbf{y}$ and $\mathbf{z}$ axes, as well as the origin $\mathbf{o} = (0,0,0)$ of the laboratory frame, lie on the focal plane, while the $\mathbf{x}$ axis is directed toward the observer. The reference frame of the *Euglena* is determined by the time-dependent unit vectors $\mathbf{i}(t)$, $\mathbf{j}(t)$, and $\mathbf{k}(t)$. The vector $\mathbf{k}(t)$ is aligned with the major axis of the ellipsoidal body of the *Euglena*, and it is directed toward the flagellum. The vector $\mathbf{i}(t)$ is defined so that the eyespot point $\mathbf{e}(t)$ lies on the plane generated by $\mathbf{i}(t)$ and $\mathbf{k}(t)$. That is, there are two (positive) constants e_i and e_k such that

$$\mathbf{e}(t) = \mathbf{i}(t)e_i + \mathbf{k}(t)e_k + \mathbf{c}(t). \qquad \textbf{[S13]}$$

The center $\mathbf{c}$ of the reference frame, as stated in the main text, is located at the geometric center of the ellipsoidal body of the cell.

To parameterize the helical trajectory of the center $\mathbf{c}$ we introduce a "helix reference frame" with origin $\mathbf{o}_h$ and orientation determined by three orthogonal unit vectors $\mathbf{l}$, $\mathbf{m}$, and $\mathbf{n}$ (Fig. S1). The vector $\mathbf{n}$ defines the helix axis. We suppose that $\mathbf{o}_h$, $\mathbf{n}$, and $\mathbf{m}$ lie on the focal plane (a hypothesis which is a posteriori justified by the good agreement between our model and the experimental data), thus $\mathbf{o}_h = (0, o_y, o_z)$. The vector $\mathbf{l}$ is aligned with the $\mathbf{x}$ axis. The angle θ_n, formed by $\mathbf{n}$ and the horizontal, determines the orientation of the frame completely.

We can write the general solution for $\mathbf{c}$ in terms of cylindrical coordinates with respect to the helix reference frame as follows:

$$\mathbf{c}(t) = \mathbf{o}_h + \rho(t)\left(\mathbf{l}\cos\psi(t) + \mathbf{m}\sin\psi(t)\right) + \mathbf{n}\zeta(t) \quad \text{with}$$
$$\rho(t) = \tilde{\rho}_b(t), \quad \psi(t) = \Delta\psi\, t/T_b + \tilde{\psi}_b(t), \quad \text{and} \quad \zeta(t) = \Delta\zeta\, t/T_b + \tilde{\zeta}_b(t), \qquad \textbf{[S14]}$$

where $\Delta\psi$ and $\Delta\zeta$ are constants, while $\tilde{\rho}_b$, $\tilde{\psi}_b$, and $\tilde{\zeta}_b$ are T_b-periodic functions. The center $\mathbf{c}$ of the body lies in the plane spanned by $\mathbf{l}$ and $\mathbf{m}$ at time $t=0$, so that

$$\zeta(0) = 0. \qquad \textbf{[S15]}$$

We parametrize the general solution for the rotation $\mathbf{R}(t) = (\mathbf{i}(t)|\mathbf{j}(t)|\mathbf{k}(t))$ of the body frame as

$$\mathbf{R}(t) = \mathbf{R}_\mathbf{n}(\alpha(t))\mathbf{R}_\mathbf{m}(\beta(t))\mathbf{R}_\mathbf{n}(\gamma(t))\mathbf{U}(\theta_n) \quad \text{with}$$
$$\alpha(t) = \Delta\psi t/T_b + \tilde{\alpha}_b(t), \quad \beta(t) = \tilde{\beta}_b(t), \quad \text{and} \quad \gamma(t) = \tilde{\gamma}_b(t), \qquad \textbf{[S16]}$$

where $\mathbf{U}(\theta_n) = \mathbf{R}_\mathbf{l}(\theta_n - \pi/2)$, while $\tilde{\alpha}_b$, $\tilde{\beta}_b$, and $\tilde{\gamma}_b$ are T_b-periodic functions.

In the remainder of this section we show how to determine the following list of parameters

$$\xi = \{T_b,\, \mathbf{o}_h,\, \theta_n,\, \Delta\psi,\, \Delta\zeta,\, \mathcal{F}\} \cup \{e_i,\, e_k\} \qquad \textbf{[S17]}$$

which describes completely the cell-body kinematics. The coefficients e_i and e_k, defined in Eq. **S13**, are auxiliary parameters needed to determine the other ones which, in turn, determine the time evolution of **c** and **R**. In Eq. **S17** we have denoted by $\mathcal{F}$ the set of Fourier coefficients of the T_b-periodic functions defined in Eqs. **S14** and **S16**. We consider only Fourier coefficients up to order one, thus

$$\begin{aligned}
\tilde{\rho}_b(t) &= a_\rho + b_\rho \cos\left(2\pi t/T_b - \phi_\rho\right), \quad & \tilde{\psi}_b(t) &= a_\psi + b_\psi \cos\left(2\pi t/T_b - \phi_\psi\right) \\
\tilde{\zeta}_b(t) &= a_\zeta + b_\zeta \cos\left(2\pi t/T_b - \phi_\zeta\right), \quad & \tilde{\alpha}_b(t) &= a_\alpha + b_\alpha \cos\left(2\pi t/T_b - \phi_\alpha\right) \\
\tilde{\beta}_b(t) &= a_\beta + b_\beta \cos\left(2\pi t/T_b - \phi_\beta\right), \quad & \tilde{\gamma}_b(t) &= a_\gamma + b_\gamma \cos\left(2\pi t/T_b - \phi_\gamma\right).
\end{aligned} \tag{S18}$$

Every Fourier coefficient is taken as an independent parameter except those of $\tilde{\zeta}_b$, since the condition in Eq. **S15** imposes $a_\zeta = -b_\zeta \cos(\phi_\zeta)$.

To obtain values for the parameters in Eq. **S17**, we fit our model to experimental data. We track the centroid and the orientation of the cell body's segmented image. Given the ellipsoidal symmetry of the cell, we interpret these data respectively as $\Pi\mathbf{c}$ and θ, where $\Pi\mathbf{k} = (\cos\theta, \sin\theta)$. Image segmentation of the eyespot give us the tracking data for $\Pi\mathbf{e}$. As in the main text, we denote by Π the projection on the focal plane. From Eqs. **S13**, **S14**, and **S16** we have that

$$\begin{aligned}
\theta(t) &= \theta_n - \arctan\left(\sin\alpha(t)\tan\beta(t)\right), \\
\Pi\mathbf{c}(t) &= \begin{pmatrix} o_y \\ o_z \end{pmatrix} + \begin{pmatrix} \sin\theta_n \\ -\cos\theta_n \end{pmatrix} \rho(t)\sin\psi(t) + \begin{pmatrix} \cos\theta_n \\ \sin\theta_n \end{pmatrix} \zeta(t), \\
\Pi\mathbf{e}(t) &= \Pi\mathbf{i}(t)\, e_i + \Pi\mathbf{k}(t)\, e_k + \Pi\mathbf{c}(t)
\end{aligned} \tag{S19}$$

where

$$\Pi\mathbf{i} = \begin{pmatrix} \sin\theta_n \\ -\cos\theta_n \end{pmatrix} (\sin\alpha\cos\beta\cos\gamma + \cos\alpha\sin\gamma) - \begin{pmatrix} \cos\theta_n \\ \sin\theta_n \end{pmatrix} \sin\beta\cos\gamma$$

$$\text{and} \quad \Pi\mathbf{k} = \begin{pmatrix} \sin\theta_n \\ -\cos\theta_n \end{pmatrix} \sin\alpha\sin\beta + \begin{pmatrix} \cos\theta_n \\ \sin\theta_n \end{pmatrix} \cos\beta.$$

From all of the definitions above, we obtain the expressions $\theta(\xi, t)$, $\Pi\mathbf{c}(\xi, t)$, and $\Pi\mathbf{e}(\xi, t)$ of our measured quantities in terms of the kinematic parameters ξ. We then obtain an estimate of the parameters ξ in three steps.

The quantities θ, $\Pi\mathbf{c}$, and $\Pi\mathbf{e}$ depend on subsets of ξ, which we denote by ξ_θ, ξ_c, and ξ_e, respectively. We first calculate the subset of nine parameters $\xi_I := \xi_\theta$. Written in full,

$$\xi_I = \{T_b,\ \theta_n,\ \Delta\psi,\ a_\alpha,\ b_\alpha,\ \phi_\alpha,\ a_\beta,\ b_\beta,\ \phi_\beta\}.$$

We obtain an estimate ξ_I^* of such parameters by solving numerically the following minimization problem:

$$\xi_I^* = \underset{\xi_I}{\operatorname{argmin}} \sum_j \left| \theta(\xi_I, t_j^\theta) - \theta^*(t_j^\theta) \right|^2. \tag{S20}$$

In the right-hand side of Eq. **S20** we have denoted with an asterisk the tracking data, and by $\{t_j^\theta\}$ the time instants where tracking data are available (analogous notation is used systematically in the following). The second subset of parameters we calculate is the difference between sets $\xi_{II} := \xi_c \setminus \xi_I$, which consists of 11 elements:

$$\xi_{II} = \{\mathbf{o}_h,\ \Delta\zeta,\ a_\rho,\ b_\rho,\ \phi_\rho,\ a_\psi,\ b_\psi,\ \phi_\psi,\ b_\zeta,\ \phi_\zeta\}.$$

We obtain an estimate ξ_{II}^* of these parameters by solving

$$\xi_{II}^* = \underset{\xi_{II}}{\operatorname{argmin}} \sum_j \left\| \Pi\mathbf{c}(\xi_{II}, \xi_I^*, t_j^c) - \Pi\mathbf{c}^*(t_j^c) \right\|^2. \tag{S21}$$

Finally, the last subset of five parameters,

$$\xi_{III} = \{e_i,\ e_k,\ a_\gamma,\ b_\gamma,\ \phi_\gamma\},$$

where $\xi_{III} := \xi_e \setminus (\xi_I \cup \xi_{II})$, is calculated by solving

$$\xi_{III}^* = \underset{\xi_{III}}{\operatorname{argmin}} \sum_j \left\| \Pi\mathbf{e}(\xi_{III}, \xi_{II}^*, \xi_I^*, t_j^e) - \Pi\mathbf{e}^*(t_j^e) \right\|^2. \tag{S22}$$

Collecting the results from Eqs. **S20–S22** we obtain all the parameters $\xi^* = \xi_I^* \cup \xi_{II}^* \cup \xi_{III}^*$ needed to fully reconstruct the time evolution of **c** and **R**. The three-step fitting procedure is devised to minimize the number of parameters to be calculated at every step. The eyespot tracking data are only needed to recover 5 parameters (out of 25). The data for $\Pi\mathbf{e}$ are fewer than the ones for $\Pi\mathbf{c}$ and θ (41 to 48 data points, depending on the experiment), but they always outnumber the free parameters to be calculated.

We end this section with a few comments. First, notice that θ depends only on the Euler angles α and β (Eq. **S19**). Solving Eq. **S22** is then crucial to find the third angle γ, which enables us to recover the rotation **R** (see the discussion in the main text). Second, from Eq. **S19** we have that $\Pi\mathbf{c}$ and θ are invariant under the transformations $\psi \mapsto \pi - \psi$ and $\alpha \mapsto \pi - \alpha$, respectively. This ultimately leads to an ambiguity on the sign of $\Delta\psi$, which in turn determines the sign of the angle γ. The two cases correspond to one motion of the moving frame and to its reflection with respect to the focal plane. In our experiments, the choice of the sign of $\Delta\psi$ was based on a visual check on the motion of the eyespot during rotation (exploiting the opacity of the cell). Rotation direction is further confirmed by its consistency with the out-of-plane motion of tracer particles near cells' bodies, which we estimated through their image changes induced by defocusing and optical aberrations (32).

3. Reconstruction of the Flagellar Shapes: Implementation Details

As stated in the main text we have, for every phase $\tau \in [0, T_b]$, a set of N_{pl} planes, each of which contains a set of points where we can locate the flagellum projection. For every plane $j = 1, \ldots, N_{pl}$, we denote by P_j^* the set of experimental points and by N_j the number of points in the set. We denote by $\mathbf{p}_{ij}^*$ the points in P_j^*, with $i = 1, \ldots, N_j$. With the definitions given in the main text, the expression for the projection error in Eq. **3** becomes

$$Err(\mathbf{r}) = \sum_{j=1}^{N_{pl}} \sum_{i=1}^{N_j} \mathrm{dist}\big(\mathbf{p}_{ij}^*, \Pi_j \mathbf{r}\big)^2 = \min_{\{s_{ij}\}} \sum_{j=1}^{N_{pl}} \sum_{i=1}^{N_j} \|\mathbf{p}_{ij}^* - \Pi_j \mathbf{r}(s_j^i)\|^2,$$

where $\mathbf{r}$ is a 3D curve. A curve $\mathbf{r}$ describes the flagellum (at phase τ) if it minimizes the projection error. To find the flagellum we take $\mathbf{r}(s) = Sp(s; \mathbf{x}_1, \ldots, \mathbf{x}_{N_{sp}})$ as in Eq. **4**, where Sp is a cubic spline defined for $s \in [0, 1]$ and interpolating N_{sp} points $\mathbf{x}_1, \ldots, \mathbf{x}_{N_{sp}}$. The nodes relative to the interpolation points are equispaced on $[0, 1]$. The starting point $\mathbf{x}_1$, determining the flagellum attachment with the ellipsoidal body, is the same for every flagellar phase, and it is fixed a priori. We solve numerically

$$\underset{\{s_{ij}\}, \mathbf{x}_1, \ldots, \mathbf{x}_{N_{pt}}}{\mathrm{argmin}} \sum_{j=1}^{N_{pl}} \sum_{i=1}^{N_j} \|\mathbf{p}_{ij}^* - \Pi_j Sp(s_{ij}; \mathbf{x}_1, \ldots, \mathbf{x}_{N_{pt}})\|^2 \qquad \textbf{[S23]}$$

to find the remaining interpolation points $\mathbf{x}_2, \ldots, \mathbf{x}_{N_{sp}}$, together with the auxiliary variables s_{ij}. We allow for the number N_{sp} of interpolating points to vary from phase to phase. Similarly, we allow for the boundary conditions to vary from phase to phase, in order for the minimization algorithm to converge. We do not impose constraints on the length of the curve $\mathbf{r}$, which is an outcome of the algorithm. As a result, lengths tend to vary slightly for different phases.

4. Uncertainties of the Reconstruction Procedure and Variability of Results

We report here the results of our body kinematics reconstruction for six different experimental datasets. Three of them, denoted Cell1a*, Cell1b, and Cell1c, correspond to the same specimen (Cell1) observed at different times (a, b, and c). The dataset Cell1a* is the one we relied on for the results presented in the main text. The other three datasets, denoted Cell2, Cell3, and Cell4, correspond to three different cells (so, four different specimens in total are analyzed).

The resulting best fits of our kinematic model for each set are shown in Fig. S2, superimposed on experimental data. Tables S1–S3 present the results of the three-step fitting procedure described in *Supporting Information*, section 2. Values of the fitted parameters are reported together with their relative (95%) confidence bounds. All fits are obtained on time intervals in which the cell completes one turn of its helical trajectory (while our observations cover typically approximately three turns).

Comparing different observations a, b, and c of the same specimen (Cell1), the motion characteristics are quite reproducible (although some variability emerges). Some kinematic quantities are also common to different specimens. All of the helical trajectories observed are quite narrow (see the average radius a_ρ). The beating period T_b oscillates around 25 ms. Also, the displacement Δz after one beat along the helix axis shows small variability. This is not quite the case for the body rotation angle after one beat $\Delta\psi$. As a consequence, the total number $N = 2\pi/\Delta\psi$ of beats needed to close a full body rotation (or, equivalently, a turn of the helical trajectory) varies from $N \approx 21$ for Cell1a* to $N \approx 35$ for Cell4. Interestingly, however, we always recover positive values for $\Delta\psi$. That is, cells always appear to rotate clockwise.

We also report the results of one additional flagellar beat reconstruction. Fig. S3 shows a comparison between the reconstructed flagellar shapes of Cell1a* and those of Cell2. This allows us to appreciate in 3D an example of the (slight) variability of the flagellar beat between cells, but also the consistency of the flagellar beating style. The uncertainties of our reconstruction procedure (for both Cell1a* and Cell2) are quantified by confidence intervals. Tables S4 and S5 present the confidence intervals for the interpolation points' coordinates of the splines that describe the flagellum (we also report the different estimated lengths of the flagellum at each phase; cf. *Supporting Information*, section 2). While most of the confidence intervals are quite narrow, some of them reveal large uncertainties. This is due to the occasional scarcity of experimental data, leading to divergent values of the confidence bounds, which are, however, confined to some small portion of the flagellum, at one particular phase.

The reconstructed flagellum of Cell1a* is compared with the experimental data in Fig. S4. For both flagellar reconstructions we consider data from a time range of ~ 21 beats. In the case of Cell1a* this corresponds to one complete turn of the helical trajectory, while for Cell2 it corresponds to *ca*. three-quarters of a turn.

We give an estimate of the variability of the flagellar beat among different observations also in a more quantitative way. We use the reconstructed 3D flagellar shapes of Cell1a* and the image data from the other five datasets. The reconstructed time history of flagellar shapes from Cell1a*, conveniently scaled in both space and time, is attached to the other cells' bodies (we use here our results from the body kinematics reconstruction). Then, the projections on the focal plane of these flagellar shapes are superimposed on the experimental images (Fig. S5 and Movie S4). A good overlap clearly emerges, showing that Cell1a* is a valid representative of a common beating style. To make the comparison quantitative we calculate the "standard projective error" σ between the reconstructions and the experimental data. The error σ is defined as follows. We consider time intervals spanning $\gtrsim 20$ flagellar beats. For each time frame in the interval, we obtain from the segmentation of microscopy images a set of points where the projection of the cell flagellum is visible. We then calculate the distances $\{d_i\}$ of each point to the projection of the reconstructed flagellum. The standard projection error is then defined as

$$\sigma = \sqrt{\frac{\sum_i d_i^2}{N_{pts}}},$$

where N_{pts} is the total number of points considered. The standard projection errors obtained for each dataset (given in terms of percentage of the flagellar length) are reported in Fig. S5 and range between 2.1% and 8.9%.

5. Physical Consistency Test for the Reconstructed Kinematics

In the present section we show that our kinematics reconstruction is consistent with the underlying physics of the system, namely, low Reynolds number hydrodynamics. We use the reconstructed flagellar shapes from Cell1a* (conveniently regularized) to calculate the body motion that results if we impose the force and torque balance (Eq. **S3**). We then compare the calculated motion with the one recorded in the experiments.

We rely on some simplifying assumptions. The hydrodynamic forces acting on the flagellum are calculated using RFT (9). With this hypothesis, the viscous force acting on the flagellum depends on two "resistive" coefficients, $C_\perp$ and $C_{//}$. More precisely, the linear density force $\mathbf{f}(s,t)$ acting on the point of the flagellum $\mathbf{r}(s,t)$ at time t and arc length s is given by

$$\mathbf{f}(s,t) = -C_\perp \mathbf{v}_\perp(s,t) - C_{//}\mathbf{v}_{//}(s,t),$$

where $\mathbf{v}_{//}(s,t) = \frac{\partial \mathbf{r}}{\partial s}(s,t) \cdot \frac{\partial \mathbf{r}}{\partial t}(s,t)$ and $\mathbf{v}_\perp(s,t) = \frac{\partial \mathbf{r}}{\partial t}(s,t) - \mathbf{v}_{//}(s,t)$ are the local velocity components parallel and perpendicular to the flagellum. The total viscous force $\mathbf{f}_{flag}$ and torque $\mathbf{g}_{flag}$ acting on the flagellum are then given by

$$\mathbf{f}_{flag} = \int_0^L \mathbf{f}(s,t)\, ds \quad \text{and} \quad \mathbf{g}_{flag} = \int_0^L (\mathbf{r}(s,t) - \mathbf{c}(t)) \times \mathbf{f}(s,t)\, ds.$$

Resistive coefficients are known to depend heavily on the geometry of the flagellum and on its hydrodynamic interaction with external structures. No theoretical choice is available for something that resembles our case, where the flagellum beats in close proximity to the *Euglena*'s body. To get a reasonable choice for the resistive coefficients, following ref. 9, we calculate them as those which best fit the experimental data. We explain this in more detail below.

We consider the total viscous force $\mathbf{f}$ and torque $\mathbf{g}$ acting on the swimmer as given by

$$\mathbf{f} = \mathbf{f}_{body} + \mathbf{f}_{flag} \quad \text{and} \quad \mathbf{g} = \mathbf{g}_{body} + \mathbf{g}_{flag},$$

where $\mathbf{f}_{body}$ and $\mathbf{g}_{body}$ are the total force and torque acting on an ellipsoid of the same size of Cell1 (moving in an unbounded fluid). The expressions for $\mathbf{f}_{body}$ and $\mathbf{g}_{body}$ can be commonly found in the literature (see e.g., ref. 31). Imposing the force and torque balance Eq. **S3**, we then obtain an expression of the type **S6**, where the right-hand side depends only on our flagellar beat reconstruction. This allows us to calculate the velocities $\bar{\mathbf{v}}(C_\perp, C_{//}, t)$ and $\bar{\boldsymbol{\omega}}(C_\perp, C_{//}, t)$ (definitions and notations taken from *Supporting Information*, section 1). Denoting by $\bar{\mathbf{v}}^*(t)$ and $\bar{\boldsymbol{\omega}}^*(t)$ the velocities that we obtain from our experiments, we define the optimal coefficients as

$$(C_\perp^*, C_{//}^*) = \underset{C_\perp, C_{//}}{\operatorname{argmin}} \int_0^{T_b} \nu_1 \|\bar{\mathbf{v}}(C_\perp, C_{//}, t) - \bar{\mathbf{v}}^*(t)\|^2 + \nu_2 \|\bar{\boldsymbol{\omega}}(C_\perp, C_{//}, t) - \bar{\boldsymbol{\omega}}^*(t)\|^2 dt$$

for conveniently chosen normalization constants ν_1 and ν_2. We take the velocities $\bar{\mathbf{v}}(C_\perp^*, C_{//}^*, t)$ and $\bar{\boldsymbol{\omega}}(C_\perp^*, C_{//}^*, t)$ as the ones that best describe the kinematics generated by the flagellar beat under the hydrodynamic force balance condition. Rotations and translations of the cell body are then calculated by time integration (**S7**). The velocities and trajectories that we obtain from the flagellar beat are compared with the experimental ones in Fig. S6.

We have a qualitative agreement (which confirms that the time sequence of reconstructed flagellar shapes is consistent with the observed swimming motion) but we are not able to reproduce all observations in full quantitative detail. Moreover, we emphasize that our estimates for the optimal resistive coefficients lead to quite nonstandard values. Indeed, if we compare them with those measured for sperm cells' flagella swimming in free space (9) our value for $C_\perp^* \approx 3.1$ fN s μm^{-2} is *ca*. 2.5 times larger and the ratio $C_\perp^*/C_{//}^* \approx 21.7$ is slightly more than one order of magnitude larger. This large discrepancy, however, is not too surprising in view of theoretical studies (33) on resistive coefficients for flagella near boundaries and of the fact that the large cell body can be seen as a (moving) wall near the beating flagellum. Clearly, our analysis represents a very crude way to encode the nonlocal hydrodynamic interactions between flagellum and cell body, and a more detailed study will be necessary in the future.

As a final remark, it is worth noticing that the values of the optimal resistive coefficients are compatible with those of a smooth flagellum. This is not a trivial outcome. The *Euglena*'s flagellum, like that of most algae, is not smooth but it is rather coated with thin, hair-like structures called mastigonemes (29). Stiff (tubular) mastigonemes are known to affect flagellar thrust in a major way, to the point of inverting the direction of resulting body motion. For example, the flagellum of *Ochromonas malhamensis* propels the cell in the same direction of the one of flagellar wave propagation (30). This does not seem to happen in the case of euglenid flagellar swimming, as can be inferred by comparing body velocities and flagellar shape evolution (Movie S5). When the flagellar wave propagates parallel to the major axis of the body we observe a peak in the translational velocity of the cell in the opposite direction (light-red to black phases in Fig. 5*E*). During the swing around the body (red to dark-blue phases), the cell counterrotates, and the angular velocity peaks. Both angular and translational velocities decrease when a wave is fading at the distal end of the flagellum, and a new one is emerging from the cell body attachment.

It has been conjectured (29) that the soft (nontubular) mastigonemes of the euglenid flagellum do not invert the flagellar thrust mechanism. Our results provide further evidence to support this claim.

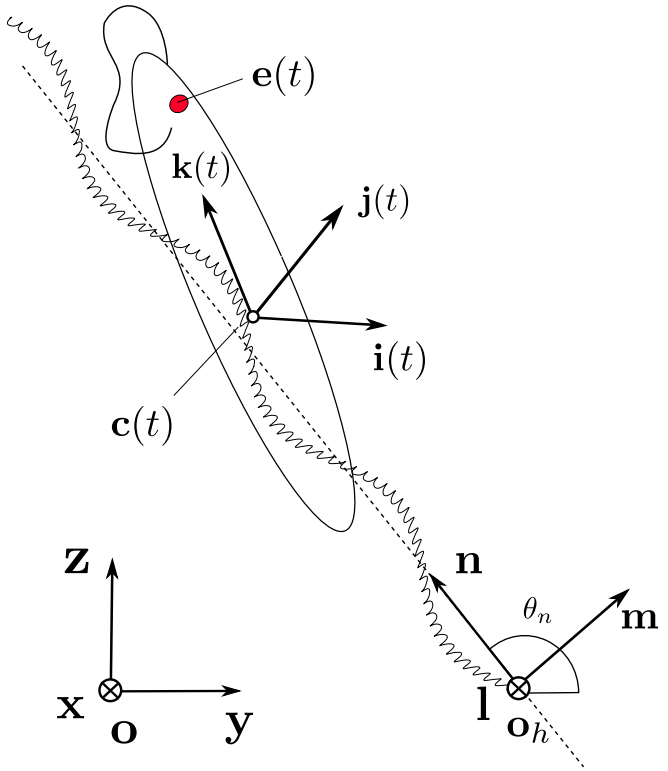

Fig. S1. Schematic description of the *Euglena*'s body kinematics. Laboratory, helix, and body reference frames are shown.

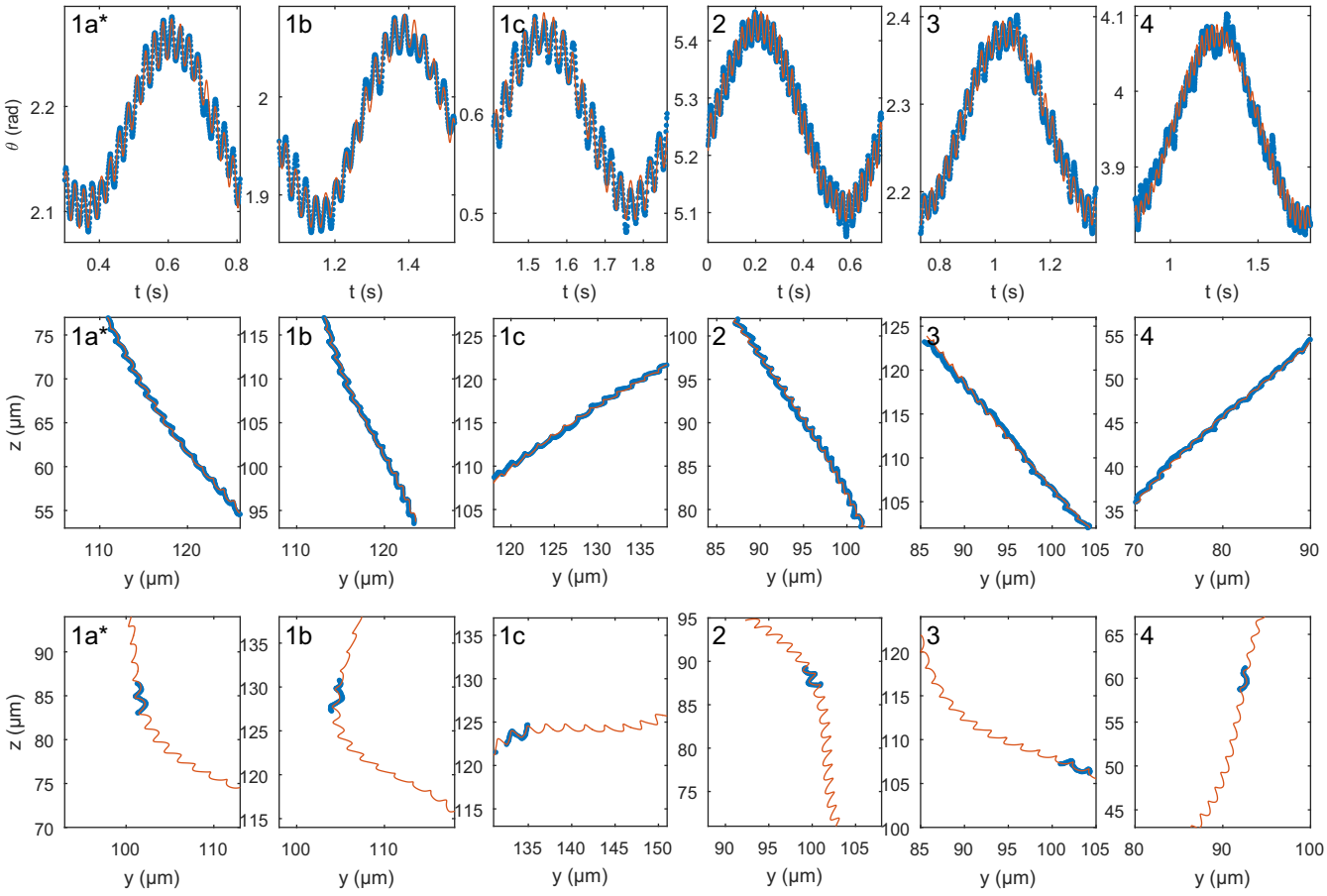

Fig. S2. Experimental data (blue points) and best fits (red line) for the quantities θ (*Top*), Π**c** (*Middle*), and Π**e** (*Bottom*).

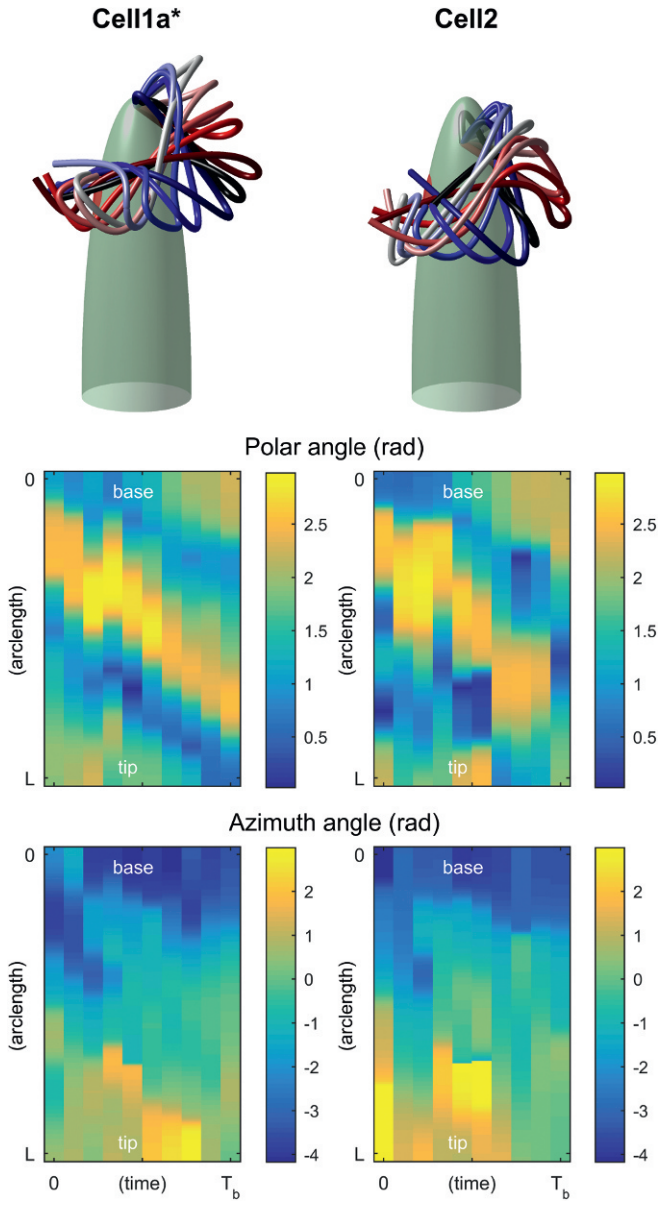

Fig. S3. Comparison between the reconstructed flagellar shapes for Cell1a* (*Left*) and Cell2 (*Right*). Sequence of flagella during the 10 phases (*Top*). Polar angle (*Middle*) and azimuth angle (*Bottom*) of the unit tangent vector to the flagella, as functions of arc length and time.

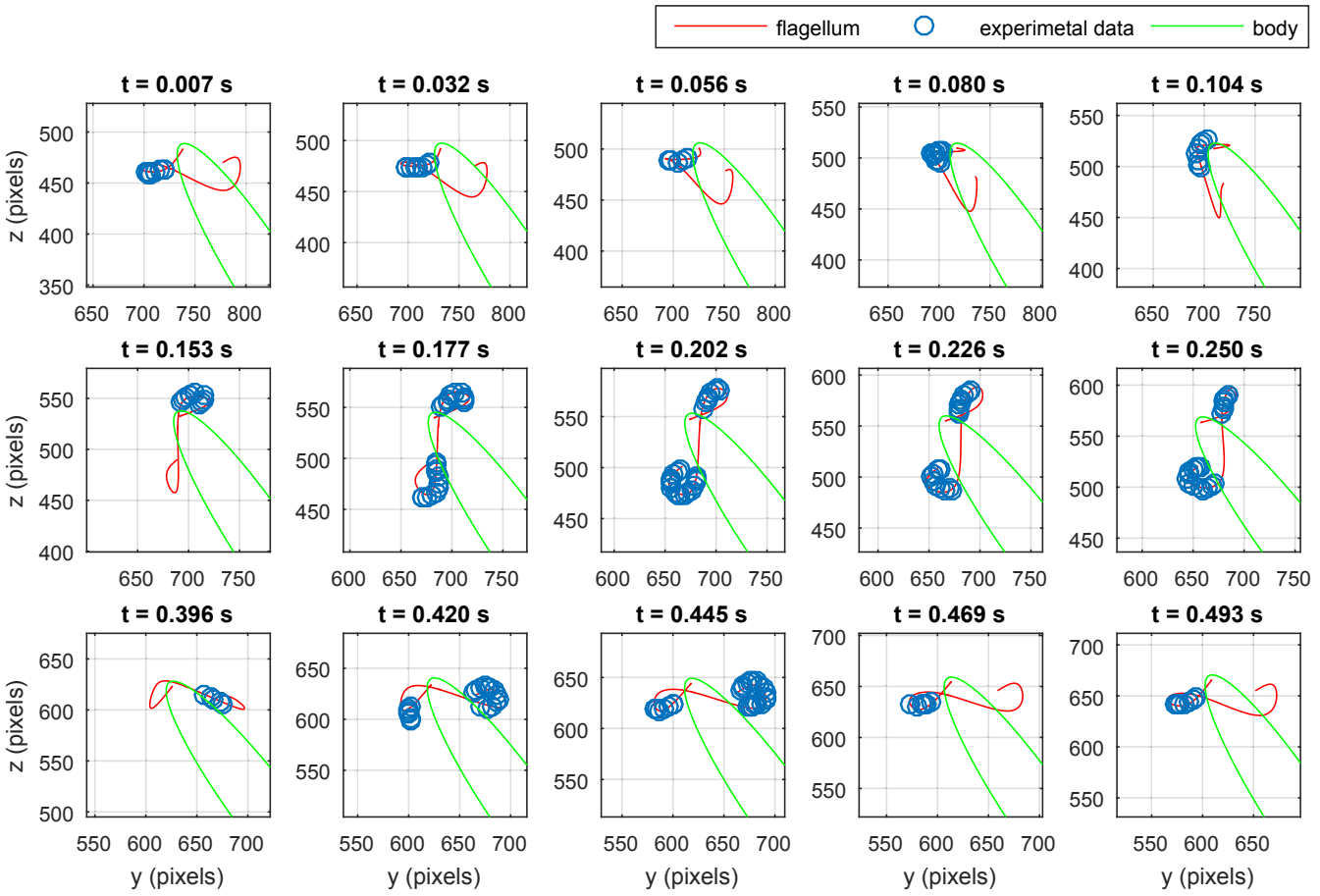

Fig. S4. Frames taken at times $t_k = \tau + kT_b$ for a fixed phase τ. The flagellum lies in the same configuration with respect to the body frame but is seen from different viewpoints. Images show the projection of the reconstructed flagellar shape (in red) superimposed on experimental data (blue circles).

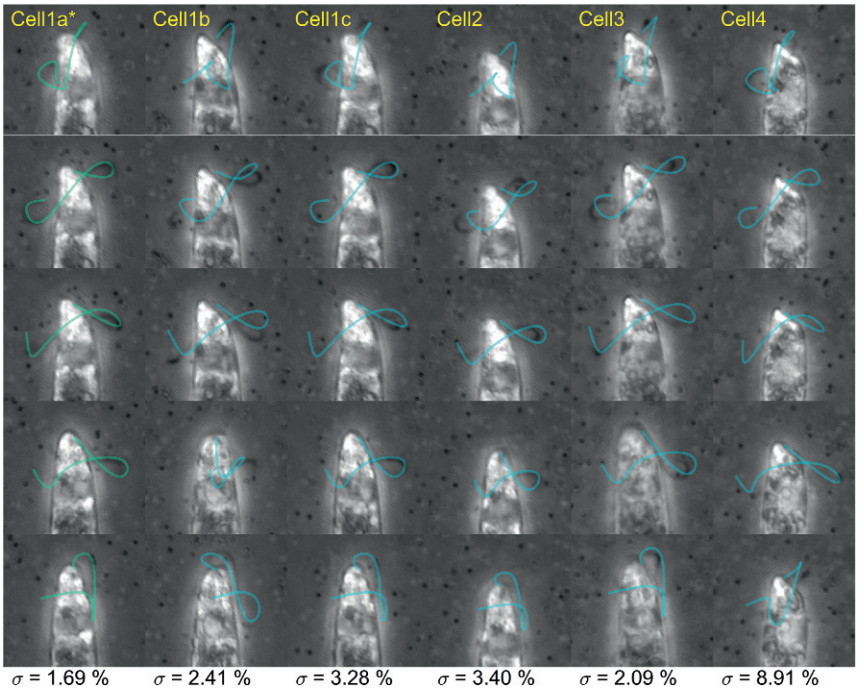

Fig. S5. The reconstructed flagellum from Cell1a* (green), conveniently scaled in both space and time, is superimposed on experimental images from other trials (blue). The standard projection error σ is also shown.

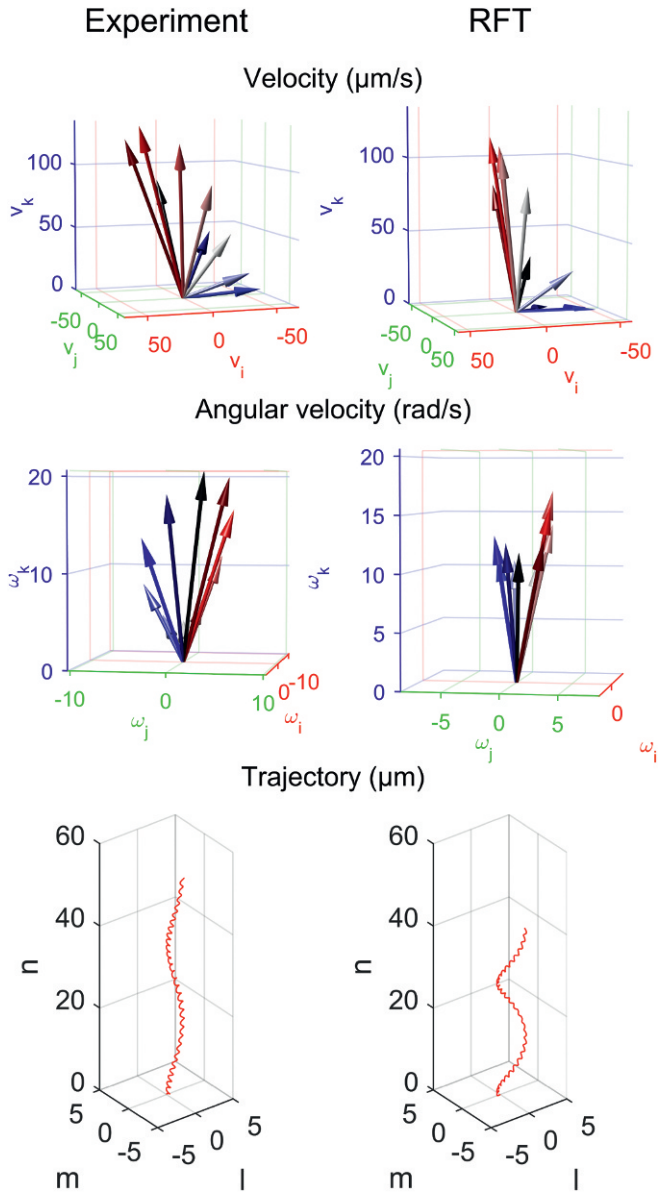

Fig. S6. Comparison between experiments (*Left*) and results obtained using RFT (*Right*): velocity vectors (*Top*), angular velocity vectors (*Middle*), and trajectory (*Bottom*).

Table S1. Parameter values with confidence bounds obtained by fitting θ

	Parameter value (±95% confidence bounds)					
Parameter	Cell1a*	Cell1b	Cell1c	Cell2	Cell3	Cell4
θ_n, rad	2.18	1.97	0.60	5.27	2.28	3.95
	(1.6e-04)	(1.5e-04)	(1.9e-04)	(1.8e-04)	(2.8e-04)	(3.3e-04)
$\Delta\psi$, rad	0.30	0.33	0.33	0.22	0.25	0.18
	(4.8e-04)	(4.0e-04)	(5.5e-04)	(1.9e-04)	(5.9e-04)	(4.1e-04)
T_b, ms	24.30	25.28	23.84	25.49	24.89	27.99
	(6.4e-03)	(9.1e-03)	(9.2e-03)	(4.7e-03)	(6.8e-03)	(8.2e-03)
a_α, rad	3.44	5.21	2.16	2.90	0.75	3.07
	(1.2e-02)	(2.1e-02)	(3.8e-02)	(3.0e-03)	(2.6e-02)	(1.9e-02)
b_α, rad	0.22	0.20	0.25	0.18	0.18	0.10
	(3.1e-03)	(3.2e-03)	(4.4e-03)	(2.3e-03)	(2.7e-03)	(2.8e-03)
ϕ_α, rad	5.48	4.50	2.22	2.68	0.28	0.21
	(4.3e-02)	(1.2e-01)	(1.7e-01)	(2.0e-02)	(7.4e-02)	(9.0e-02)
a_β, rad	0.08	0.09	0.08	0.16	0.10	0.12
	(1.8e-04)	(2.1e-04)	(2.7e-04)	(2.6e-04)	(2.2e-04)	(2.7e-04)
b_β, rad	0.02	0.02	0.02	0.03	0.02	0.01
	(2.5e-04)	(3.0e-04)	(3.7e-04)	(3.7e-04)	(2.7e-04)	(3.4e-04)
ϕ_β, rad	0.57	5.86	3.82	4.52	1.86	1.29
	(3.8e-02)	(1.1e-01)	(1.7e-01)	(2.3e-02)	(7.5e-02)	(9.2e-02)

Table S2. Parameter values with confidence bounds obtained by fitting Πc

	Parameter value (±95% confidence bounds)					
Parameter	Cell1a*	Cell1b	Cell1c	Cell2	Cell3	Cell4
h_y, μm	138.78	150.11	28.92	84.47	147.47	143.76
	(1.3e-02)	(1.5e-02)	(5.8e-02)	(5.6e-03)	(2.4e-02)	(2.0e-02)
h_z, μm	36.02	30.49	47.88	106.61	51.43	111.92
	(1.7e-02)	(3.4e-02)	(4.0e-02)	(7.8e-03)	(2.7e-02)	(2.1e-02)
Δz, μm	1.72	1.66	1.79	1.39	1.74	1.66
	(8.2e-04)	(7.2e-04)	(1.0e-03)	(4.4e-04)	(8.1e-04)	(5.6e-04)
a_ρ, μm	0.75	0.55	0.47	0.47	0.42	1.17
	(7.1e-03)	(5.5e-03)	(7.9e-03)	(5.1e-03)	(8.5e-03)	(8.2e-03)
b_ρ, μm	0.20	0.20	0.21	0.24	0.19	0.18
	(1.0e-02)	(7.8e-03)	(1.1e-02)	(7.3e-03)	(1.2e-02)	(1.2e-02)
ϕ_ρ, rad	5.83	5.18	4.44	5.55	2.55	1.08
	(4.9e-02)	(4.0e-02)	(5.4e-02)	(3.0e-02)	(6.4e-02)	(6.6e-02)
a_ψ, rad	4.76	6.16	1.68	1.55	0.08	3.40
	(1.0e-02)	(1.1e-02)	(1.9e-02)	(1.3e-02)	(2.3e-02)	(7.1e-03)
b_ψ, rad	0.26	0.27	0.43	0.47	0.46	0.09
	(1.3e-02)	(1.4e-02)	(2.4e-02)	(1.5e-02)	(2.8e-02)	(9.8e-03)
ϕ_ψ, rad	3.95	3.44	2.67	4.18	0.92	6.12
	(5.4e-02)	(5.7e-02)	(6.2e-02)	(3.8e-02)	(7.1e-02)	(1.1e-01)
b_z, μm	0.24	0.25	0.21	0.19	0.26	0.20
	(7.1e-03)	(5.5e-03)	(7.9e-03)	(5.1e-03)	(8.5e-03)	(8.2e-03)
ϕ_z, rad	0.01	5.21	2.70	3.47	0.83	1.73
	(3.0e-02)	(2.2e-02)	(3.7e-02)	(2.7e-02)	(3.3e-02)	(4.1e-02)

Table S3. Parameter values with confidence bounds obtained by fitting IIe

	Parameter value (±95% confidence bounds)					
Parameter	Cell1a*	Cell1b	Cell1c	Cell2	Cell3	Cell4
e_k, μm	16.98 (9.1e-03)	16.72 (1.8e-02)	16.73 (1.2e-02)	14.45 (1.5e-02)	17.74 (1.1e-02)	17.55 (1.5e-02)
e_i, μm	1.71 (4.8e-02)	2.66 (9.3e-02)	3.50 (5.5e-02)	2.19 (1.1e-01)	2.81 (8.5e-02)	2.99 (1.1e-01)
a_γ, rad	0.56 (2.6e-02)	0.84 (2.1e-02)	1.43 (1.6e-02)	1.23 (3.7e-02)	1.00 (4.2e-03)	0.31 (5.2e-03)
$b\gamma$, rad	0.23 (1.1e-02)	0.21 (1.2e-02)	0.28 (6.8e-03)	0.20 (1.1e-02)	0.19 (5.4e-03)	0.10 (4.2e-03)
$\phi\gamma$, rad	2.21 (4.5e-02)	1.14 (5.3e-02)	5.32 (2.6e-02)	5.72 (6.0e-02)	3.21 (2.7e-02)	3.41 (4.1e-02)

Table S4. Uncertainties of the flagellar shapes reconstruction procedure for Cell1a*

	Beat phase									
n_{sp}	$0.0T_b$	$0.1T_b$	$0.2T_b$	$0.3T_b$	$0.4T_b$	$0.5T_b$	$0.6T_b$	$0.7T_b$	$0.8T_b$	$0.9T_b$
	±95% confidence bounds for **i**-components, μm									
1	0.00	0.00	0.00	0.00	0.00	0.00	0.00	0.00	0.00	0.00
2	0.35	0.32	0.18	0.12	0.10	0.27	0.26	0.31	0.13	0.22
3	0.19	0.16	0.06	0.03	0.05	0.10	0.11	0.19	0.25	0.33
4	0.28	0.32	0.07	0.08	0.18	0.24	0.37	0.38	0.67	0.54
5	1.18	0.37	0.14	0.42	0.14	0.31	0.24	0.46	0.17	0.17
6	0.77	0.09	0.27	1.07	0.33	0.63	0.13	0.18	0.24	0.25
7	0.09		0.19	2.84	1.53		0.13	0.13		
8				322.35				0.14		
9				2,071.27						
	±95% confidence bounds for **j**-components, μm									
1	0.00	0.00	0.00	0.00	0.00	0.00	0.00	0.00	0.00	0.00
2	0.29	0.21	0.18	0.07	0.08	0.28	0.16	0.46	0.17	0.18
3	0.25	0.17	0.08	0.12	0.10	0.13	0.29	0.16	0.19	0.21
4	0.27	0.22	0.10	0.12	0.14	0.10	0.28	0.27	0.17	0.34
5	1.40	0.36	0.06	0.66	0.10	0.13	0.17	0.19	0.26	0.43
6	0.47	0.23	0.37	0.20	0.29	1.00	0.13	0.17	0.29	0.36
7	0.29		0.22	9.69	1.35		0.21	0.13		
8				174.70				0.13		
9				1,051.48						
	±95% confidence bounds for **k**-components, μm									
1	0.00	0.00	0.00	0.00	0.00	0.00	0.00	0.00	0.00	0.00
2	0.42	0.31	0.11	0.07	0.08	0.09	0.04	0.07	0.05	0.12
3	0.19	0.22	0.19	0.21	0.12	0.11	0.12	0.18	0.05	0.13
4	0.34	0.27	0.10	0.55	0.24	0.10	0.41	0.05	0.52	0.33
5	0.25	0.07	0.16	0.10	0.32	0.11	0.09	0.36	0.13	0.33
6	0.40	0.08	0.10	2.80	0.09	0.11	0.09	0.07	0.09	0.15
7	0.08		0.16	0.09	0.23		0.07	0.11		
8				161.13				0.06		
9				1,080.15						
	Flagellar length, μm									
	38.9	39.1	37.9	38.7	36.5	40.1	36.9	35.7	37.7	39.6

Confidence bounds for the interpolation points' coordinates of the splines that describe the flagellum (at each phase) and estimated flagellar length.

Table S5. Uncertainties of the flagellar shapes reconstruction procedure for Cell2

	Beat phase									
n_{sp}	$0.0T_b$	$0.1T_b$	$0.2T_b$	$0.3T_b$	$0.4T_b$	$0.5T_b$	$0.6T_b$	$0.7T_b$	$0.8T_b$	$0.9T_b$
	±95% confidence bounds for **i**-components, μm									
1	0.00	0.00	0.00	0.00	0.00	0.00	0.00	0.00	0.00	0.00
2	0.39	0.14	0.09	0.08	0.06	0.10	0.22	0.09	0.13	0.30
3	0.17	0.19	0.37	0.45	0.09	0.26	0.35	0.07	0.11	0.18
4	0.51	2.61	0.49	0.25	0.44	0.42	0.43	0.19	0.42	0.24
5	0.53	3.80	0.39	0.59	0.09	0.15	0.26	0.26	1.02	0.75
6	4.57		0.16	1.45	0.14	0.19				
7	58.23		0.43		0.14					
	±95% confidence bounds for **j**-components, μm									
1	0.00	0.00	0.00	0.00	0.00	0.00	0.00	0.00	0.00	0.00
2	0.30	0.13	0.24	0.13	0.11	0.33	0.78	0.25	0.23	0.27
3	0.38	0.56	0.73	0.25	0.13	0.29	0.75	0.20	0.16	0.32
4	0.24	0.49	0.87	0.14	0.10	0.39	0.85	0.23	0.63	0.34
5	2.35	20.72	0.31	0.89	0.10	0.20	0.93	0.70	1.57	1.00
6	4.16		0.13	1.37	0.11	0.25				
7	21.80		0.38		0.34					
	±95% confidence bounds for **k**-components, μm									
1	0.00	0.00	0.00	0.00	0.00	0.00	0.00	0.00	0.00	0.00
2	0.71	0.25	0.22	0.13	0.05	0.08	0.16	0.08	0.08	0.18
3	0.26	0.60	1.87	0.29	0.13	0.19	0.23	0.07	0.06	0.33
4	0.77	2.51	0.79	0.47	0.40	0.63	0.41	0.12	0.25	0.11
5	1.80	0.83	0.16	0.25	0.18	0.27	0.89	0.12	0.16	0.21
6	4.37		0.17	0.37	0.15	0.17				
7	47.88		0.12		0.12					
	Flagellar length, μm									
	35.3	34.5	31.4	29.4	34.1	38.8	37.5	35.4	34.9	36.2

Confidence bounds for the interpolation points' coordinates of the splines that describe the flagellum (at each phase) and estimated flagellar length.

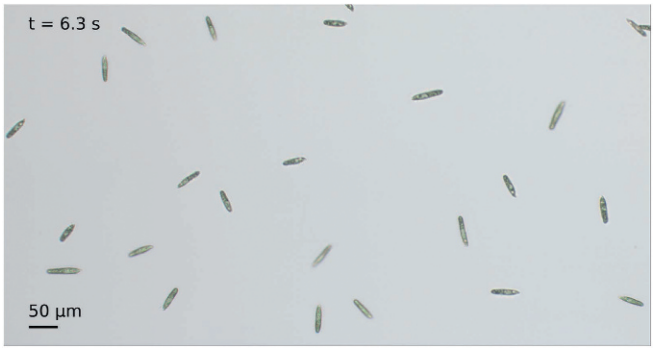

Movie S1. Montage of video recordings of swimming *E. gracilis* observed under a microscope (at increasing magnification and image-acquisition rate). At time scales larger than the flagellar beating period cells can be observed moving on a helical path while rotating about a fixed axis. At smaller time scales, finer features of the rototraslatory motion appear.

Movie S1

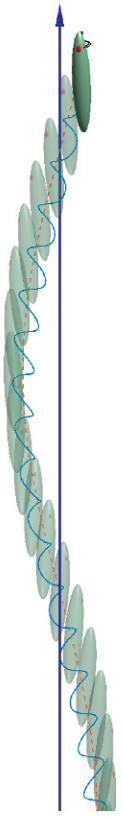

Movie S2. Reconstructed swimming kinematics of *E. gracilis*. The resulting trajectory of the cell can be seen as a smooth circular helix (the "backbone" trajectory), perturbed by periodic "swirls" at the flagellar beating time scale. The cell completes one turn of the helix while undergoing a full rotation around the axis of the helix. The *Euglena*'s body is not to scale with the displacements for visualization purposes.

Movie S2

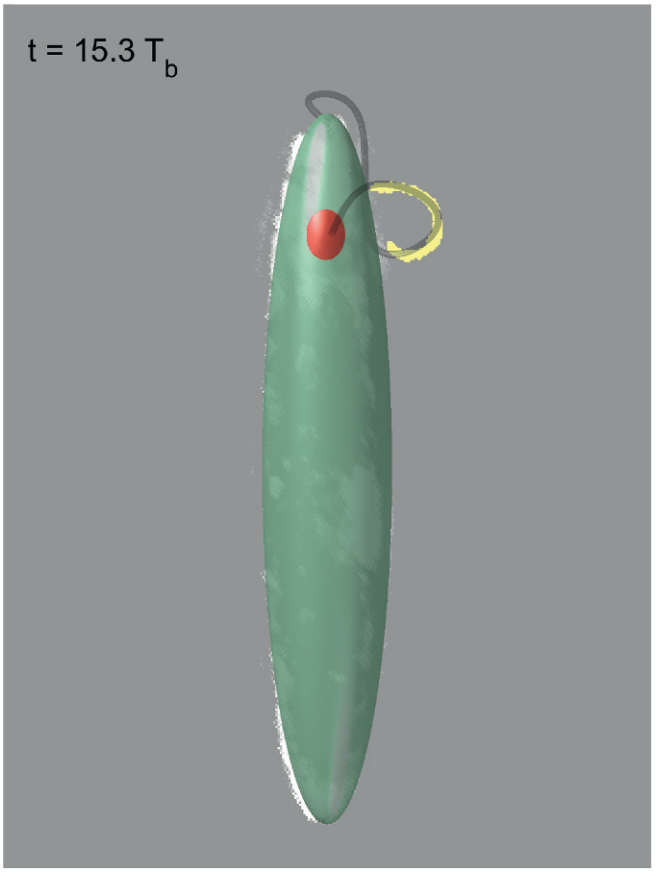

Movie S3. Flagellar shape reconstruction. We exploit the slow (incremental) rotational motion of the *Euglena* around the axis of its helical trajectory. As the *Euglena* rotates, at instants one beating period T_b apart, different views of the same flagellar configuration are exposed. This permits an algorithmic stereo matching reconstruction of the intrabeat flagellar shapes.

Movie S3

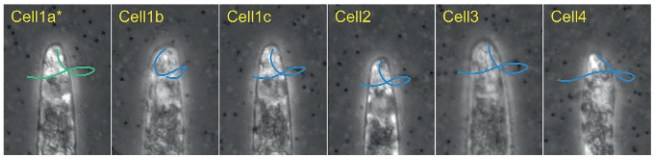

Movie S4. Variability of the flagellar beat among different observations. The reconstructed 3D flagellar shape of Cell1a* (green), conveniently scaled in both space and time, is superimposed (blue) on image data from the other five datasets. The good overlap suggests the existence of a distinctive *Euglena* beat style.

Movie S4

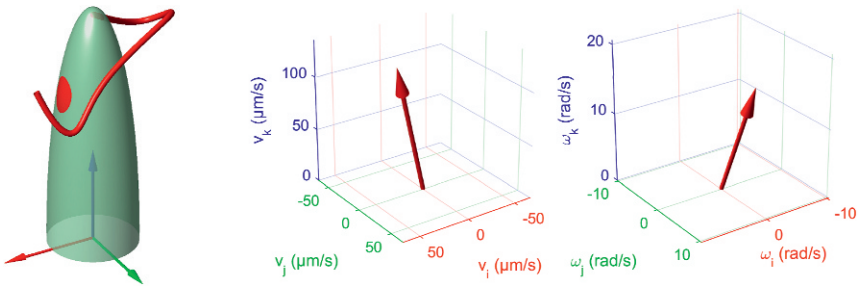

Movie S5. Comparison between flagellar shapes, during one beat, and the resulting translational and angular velocities (represented in the cell body reference frame coordinates).

Movie S5

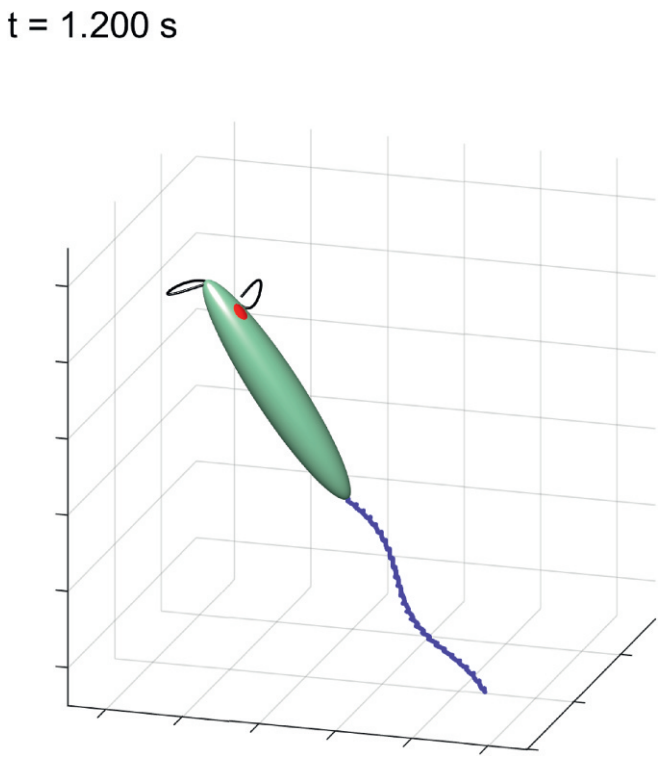

Movie S6. Video summary. Reconstruction of the 3D kinematics of euglenoid flagellar swimming, starting from high-resolution 2D image recordings.

Movie S6